Neurobiology of Disease 132 (2019) 104588

Contents lists available at ScienceDirect

Neurobiology of Disease

journal homepage: www.elsevier.com/locate/ynbdi

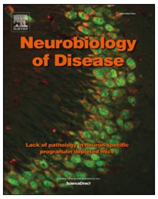

KCa3.1 deficiency attenuates neuroinflammation by regulating an astrocyte phenotype switch involving the PI3K/AKT/GSK3β pathway

Tianjiao Wei[a], Yanxia Wang[b], Weirong Xu[b], Yan Liu[b], Hongzhuan Chen[a,c,*], Zhihua Yu[a,*]

[a] Department of Pharmacology and Chemical Biology, Shanghai Jiao Tong University School of Medicine, Shanghai 200025, China
[b] Experimental Teaching Center of Basic Medicine, Shanghai Jiao Tong University School of Medicine, Shanghai 200025, China
[c] Shanghai University of Traditional Chinese Medicine, Shanghai 201203, China

ARTICLE INFO

Keywords:
KCa3.1
Orai1
Astrocytes
Insulin
Tau

ABSTRACT

Neuroinflammation may induce a phenotype switch to reactive astrogliosis in neurodegenerative disorders. The calcium-activated potassium channel (KCa3.1) is active in the phenotypic switch that occurs during astrogliosis in Alzheimer's disease and ischemic stroke. Here, transcriptome sequencing (RNA-Seq), immunohistochemistry, western blotting, pharmacological blockade, and calcium imaging were used to investigate astrocyte KCa3.1 activity in neuroinflammation, Tau accumulation, and insulin signaling deficits in male wild-type C57BL/6 and KCa3.1$^{-/-}$ knockout (KO) mice, and in primary astrocyte cultures. KCa3.1 deficiency in KO mice decreased lipopolysaccharide (LPS)-induced memory deficits, neuronal loss, glial activation, Tau phosphorylation, and insulin signaling deficits in vivo. KCa3.1 expression in astrocytes was associated with LPS-induced upregulation of the Orai1 store-operated Ca^{2+} channel protein. The KCa3.1 channel was found to regulate store-operated Ca^{2+} overload through an interaction with Orai1 in LPS-induced reactive astrocytes. The LPS-induced effects on KCa3.1 and Orai1 indirectly promoted astrogliosis-related changes via the PI3K/AKT/GSK3β and NF-κB signaling pathways in vitro. Unbiased evaluation of RNA-Seq results for actively translated RNAs confirmed that substantial astrocyte diversity was associated with KCa3.1 deficiency. Our results suggest that KCa3.1 regulated astrogliosis-mediated neuroinflammation, Tau accumulation, and insulin signaling deficiency via PI3K/AKT/GSK3β and NF-κB signaling pathways, and contributing to neuronal loss and memory deficits in this neuroinflammation mouse model.

1. Introduction

An intermediate conductance calcium-activated potassium channel, KCa3.1, regulates the intracellular Ca^{2+} concentration, $[Ca^{2+}]_i$, in astrocytes (Staal et al., 2017; Yi et al., 2017). K^+ efflux resulting from activation of the KCa3.1 channel leads to membrane hyperpolarization, which in turn facilitates Ca^{2+} influx (Schilling et al., 2004). KCa3.1 is involved in the astrogliosis phenotypic switch that occurs in both AD and ischemic stroke (Yu et al., 2017). KCa3.1 gene deletion has been found to attenuate endoplasmic reticulum (ER) stress and reactive astrogliosis via the c-Jun/JNK and ERK1/2 signaling pathways in a mouse model of ischemic stroke. Treatment of diabetic ketoacidosis by pharmacological blockade of KCa3.1 with TRAM-34 decreases reactive astrogliosis and microglial activation in agreement with a decreased inflammatory response (Glaser et al., 2017).

Astrocytes support central neurons by maintaining ATP, glucose, and glutamate homeostasis (Coulter and Eid, 2012; Lalo et al., 2014; Seifert and Steinhauser, 2013). In neurodegenerative disorders and central nervous system (CNS) injury, astrocytes undergo reactive astrogliosis, a phenotype switch characterized by neuroinflammation and impaired cellular metabolism and neurotransmitter cycling (Zamanian et al., 2012). Reactive astrogliosis has been associated with Tau phosphorylation and amyloid-beta (Aβ) peptide-induced neurotoxicity (Shapira et al., 2018). Reactive astrogliosis can produce either harmful or beneficial effects during CNS recovery from injury. Genomic analysis has identified two types of astrocytes, A1 and A2, in mouse models of

---

Abbreviations: GFAP, Glial fibrillary acidic protein; KCa3.1, Intermediate-conductance calciumactivated potassium channel; SOCE, store-operated Ca2+ entry; TRAM-34, 1-((2-chlorophenyl) (diphenyl) methyl)-1H–pyrazole; ROS, reactive oxygen species; SAMP8, senescence-accelerated mouse prone 8; EGTA, ethylene glycol-bis (β-aminoethyl ether)-N,N,N′,N′-tetraacetic acid; SDS-PAGE, sodium dodecyl sulfate-polyacrylamide gel electrophoresis; DAPI, 4′,6-diamidino-2-phenylindole.

* Corresponding authors at: Department of Pharmacology and Chemical Biology, Shanghai Jiao Tong University School of Medicine, 280 South Chongqing Road, Shanghai 200025, China.

E-mail addresses: honghzun-chen@hotmail.com, yaoli@shsmu.edu.cn (H. Chen), yuzhihua@shsmu.edu.cn (Z. Yu).

https://doi.org/10.1016/j.nbd.2019.104588
Received 11 April 2019; Received in revised form 22 July 2019; Accepted 23 August 2019

neuroinflammation induced by systemic injection of lipopolysaccharide (LPS) and ischemic stroke following middle cerebral artery ligation (Zamanian et al., 2012). LPS-induced A1 astrocytes upregulate the classical complement pathway genes, thus resulting in injury of synapses during neuroinflammation. Ischemia-induced A2 astrocytes upregulate neurotrophic factors that promote CNS recovery and repair (Sofroniew and Vinters, 2010; Zador et al., 2009). A1 astrocytes induced by activated microglia have neurotoxic functions (Liddelow and Barres, 2017; Liddelow et al., 2017). A better understanding of the phenotype switch in reactive astrocytes may contribute to the development of novel therapies to decrease neurological impairment in neurodegenerative diseases.

Impaired insulin signaling occurs in both diabetes and Alzheimer's disease (AD), where it may promote inflammation (Bomfim et al., 2012). Astrocytes are insulin responsive and uptake glucose, which is essential for neuron energy metabolism. Insulin inhibits the expression of nitric oxide synthase and oxidative damage induced by LPS and H_2O_2 in astrocytes (Ramalingam and Kim, 2014). Insulin signaling deficits lead to hyperphosphorylation of Tau and the formation of neurofibrillary tangles found in neurodegenerative disorders such as AD and Parkinson's disease (Calvo-Ochoa et al., 2014). Tau kinases, such as glycogen synthase kinase 3 beta (GSK3β), promote insulin-modulated Tau phosphorylation via the phosphatidylinositol kinase (PI3K)/protein kinase B (AKT) pathway (Flores et al., 2008; Schubert et al., 2004). Insulin resistance leads to Tau hyperphosphorylation by inhibition of AMPK-induced Tau de-phosphorylation and aberrant activation of GSK3β (Kim et al., 2015; Schubert et al., 2004).

This study investigated KCa3.1 regulation of astrogliosis-mediated neuroinflammation, Tau accumulation, and insulin signaling deficiency in astrocyte primary cultures and neuronal loss and memory deficits in an LPS-induced mouse model of neuroinflammation.

2. Material and methods

2.1. Compounds and formulations

Senicapoc (ICA-17043, TargetMol, Boston, MA) was dissolved at 100 mM in Dimethyl sulfoxide (Sigma-Aldrich, St. Louis, MO) and diluted in media for in vitro studies. For oral administration to C57BL/6 mice, senicapoc was dissolved in a cremophore EL®/water (10: 90) mixture (Calbiochem®, Merck, Darmstadt, Germany) as a concentration at 100 mg/kg. The endotoxin LPS from *Escherichia coli* O55:B55 (Sigma-Aldrich, St. Louis, MO; final concentration of 5 mg/kg in vivo) dissolved in normal saline. The LPS (final concentration of 0.1 mg/ml in vitro) was dissolved in Dulbecco's Modified Eagles Medium (DMEM, Invitrogen) and stored at −20 °C until use. SB20358, SP600125, LY294002, U0126 and 2-APB were from Tocris Bioscience (Bristol, UK).

2.2. Animals

Animal care and procedures were approved by the Animal Experimentation Ethics Committee of Shanghai Jiao Tong University School of Medicine, Shanghai, China (ethics protocol A-2015-010). KCa3.1$^{-/-}$ knockout mice (KO) were purchased from the Jackson Laboratory (stock no: 018826 B6; 129S1-Kcnn4^{tm1Jemn}/J) (Yi et al., 2017). KO male mice and their Wild-type (WT) littermates weighing 25–30 g were assigned to four groups of 15 mice each and received intraperitoneal injection of either LPS at 5 mg/kg (Zamanian et al., 2012) or an equal volume of the saline vehicle. The mice were evaluated with a water maze test 7 days after treatment and then euthanized for collection of brain tissue for western blotting assays and histological evaluation.

2.3. Morris water maze test

The spatial memory of WT and KO mice was evaluated with a modified Morris water maze test as described by Morris et al. (Morris, 1984). The test was conducted in a circular pool 120 cm in diameter and 50 cm deep, which was equipped with image pickup and video analysis systems (Shanghai Jialiang Software Technology Co, Ltd.). A 4.5 cm diameter escape platform was placed 1 cm below the water surface. To successfully complete the test, the mice were required to find the hidden platform within 60 s. Mice that did not find the platform within 60 s were placed on the platform for 10 s at the end of the testing. The water maze test included 5 days of training with a visible platform on day 1 and a hidden platform on the other 4 days, followed by a practice trial on day 6 without a platform. Each mouse performed two separate trials with the platform, which was removed on the last day. The escape latency and escape distance (the time and distance required to find the hidden platform), swimming distance and swimming time (the distance and time that the mouse remained in the target quadrant), and the time needed to cross the platform were used to evaluate learning and memory.

2.4. Immunostaining and image analysis

Brain tissue was collected, prepared, immunostained and evaluated through confocal microscopy as previously described (Yi et al., 2016a; Yi et al., 2016b). Mice were anesthetized with chloral hydrate and perfused with 4% paraformaldehyde. After embedding in paraffin, sectioning at 12 μm, and mounting, the tissue was dewaxed, rehydrated and blocked by incubation with 10% goat serum in 0.01 M phosphate-buffered saline for 1 h at room temperature. The brain sections were then incubated with rabbit anti-glial fibrillary acidic protein (GFAP, 1:1000; Dako, Glostrup, Denmark), rabbit anti-NeuN (1:100; Merck Millipore, Burlington, MA, USA), or rabbit anti-Iba1 (1:500; Wako Pure Chemical Industries, Ltd., Osaka, Japan), or mouse anti-KCa3.1 (1:100; Alomone Labs, Ltd., Jerusalem, Israel) primary antibodies overnight at 4 °C. The tissue sections were incubated with Alexa Fluor 568-conjugated secondary antibodies (1:500; Invitrogen Corporation, Carlsbad, CA, USA). Images were obtained with a TCS SP8 confocal laser scanning microscope (Leica Microsystems, Wetzlar, Germany), and the GFAP, Iba-1 or NeuN positive cell number was counted in a blinded manner, and the area was measured by Leica LAS AF Lite software (Leica, Germany). The same reference point in each brain tissue section was used for three to five 0.01 mm^2 diameter microscopic fields that were randomly selected from the same reference point in each brain tissue section for image analysis. The blinded analysis included six sections from each brain specimen separated by 120 μm intervals. For KCa3.1 immunohistochemistry, the sections were incubated with mouse anti-KCa3.1 (1:100) at 4 °C overnight. The following day, sections were treated with biotinylated anti-mouse IgG and then processed with avidin-biotin peroxidase complex. The peroxidase reaction was visualized by 0.05% DAB with 0.03% H_2O_2.

2.5. Primary astrocyte cultures

Primary mixed glial cell cultures were prepared from brain tissue collected from newborn C57BL/6 J mice (P0–P2), as previously described (Wei et al., 2016). Cerebral cortex tissue was dissociated into a single-cell suspension through treatment with 0.25% trypsin (Invitrogen) for 15 min at 37 °C and mechanical disruption. Cells were grown in DMEM plus 10% fetal bovine serum. The confluent mixed glial cell cultures that formed in 10–14 days were shaken at 200 rpm overnight at 37 °C to suspend loosely attached microglia and oligodendrocyte precursor cells. Astrocytes were then harvested by trypsinization of the remaining cells and were transferred to six-well plates. Astrocyte-conditioned medium (ACM) for neuron culture was prepared as previously described (Wei et al., 2016). Briefly, the astrocyte culture medium was changed from DMEM plus 10% fetal bovine serum to serum-free neurobasal medium (NB, Gibco) with B27 supplement (Invitrogen). Astrocytes in NB/B27 medium were treated with 10 μg/ml

LPS for 48 h, and the resulting ACM was collected, centrifuged (1200 rpm, 5 min), and filtered (0.22 μm low-protein binding filter; Millipore, Billerica, MA) to remove the cell debris and LPS. Primary neuron cultures were prepared from newborn (P0–P2) C57BL/6 mice, as described by Wei et al. (Wei et al., 2016), and cultured in NB/B27 medium for 10–14 days. A Cell Counting Kit-8 (CCK-8, Dojindo Laboratories, Kumamoto, Japan) was used to assay cell viability (Yu et al., 2013).

2.6. Neurite outgrowth assay

Primary neuron cultures were incubated with a primary antibody against microtubule associated protein 2 (MAP2, 1:1000, Abcam) and Alexa Fluor 568-conjugated secondary antibody. MAP2-positive cells were scanned with a Cellomics Kinetic Scan reader (Thermo Fisher Scientific, Waltham, MA, USA). Extended Neurite Outgrowth software (Thermo Fisher Scientific) was used for image analysis.

2.7. TNF-α and IL-1β assay

TNF-α and IL-1β protein levels were determined with enzyme-linked immunosorbent assay (ELISA) kits (Rapidbio Labs, Langka Trade Co. Ltd., Shanghai, China) according to the manufacturer's instructions.

2.8. Western blotting

Mice were anesthetized with chloral hydrate and perfused with saline. Mice brain tissues or primary cells were lysed on ice with radioimmunoprecipitation assay buffer (50 mM Tris (pH 7.4), 150 mM NaCl, 1% Triton X-100, 1% sodium deoxycholate, 0.1% sodium dodecyl sulfate, sodium orthovanadate, sodium fluoride, ethylenediaminetetraacetic acid, leupeptin) containing 1% phenylmethanesulfonyl fluoride. Equal concentrations of proteins were separated by 10% (*w/v*) sodium dodecyl sulfate-polyacrylamide gel electrophoresis and then transferred to a polyvinylidene difluoride membrane, which was blocked for 1 h at room temperature in 5% milk in Tris-buffered saline with 0.05% Tween 20. The membrane was incubated with following primary antibodies overnight at 4 °C: KCa3.1 (1:400, ab83740, Abcam), β-actin (1:3000, A1978, Sigma), Phospho-Akt Kit (1:1000, #9916), Phospho-Tau (1:1000, #9632), NF-κB p65 (1:1000, #8242), PSD95 (1:1000, #3407), Phospho-NF-κB p65 (1:1000, #3033, Cell Signaling Technology, Danvers, MA, USA), Orai1 (1:500, H-46), p-IκB-α (1:500, B-9), IκB-α (1:500, H-4), Insulin Rβ (1:1000, sc-377071, Santa Cruz Biotech.), Tau (1:1000, MAB5430, MILLPORE) and the corresponding conjugated anti-rabbit and anti-mouse IgG-horseradish peroxidase (1:2000, Santa Cruz Biotechn, Santa Cruz, CA, USA) secondary antibodies were performed for 1 h at room temperature, and developed using BeyoECL solution (P0018A; Beyotime Institute of Biotechnology). Image Studio Lite Ver 5.2 software (LI-COR Biosciences, Lincoln, NE, USA) was used to analyze the proteins.

2.9. Affinity purification of translating RNA, amplification, and sequencing library construction

Total RNA was extracted with TRIzol reagent (Invitrogen Life Technologies), and the concentration, quality, and integrity were determined with a NanoDrop spectrophotometer (Thermo Scientific). Three micrograms of RNA were used as input material for the RNA sample preparations. Sequencing libraries were generated using the TruSeq RNA Sample Preparation Kit (Illumina, San Diego, CA, USA). Briefly, mRNA was purified from total RNA with poly-T oligonucleotide-attached magnetic beads. Fragmentation was carried out at an elevated temperature in a proprietary Illumina fragmentation buffer containing divalent cations. The first strand cDNA was synthesized with random oligonucleotides and SuperScript II. Second strand cDNA synthesis was performed with DNA Polymerase I and RNase H. The remaining overhangs were converted to blunt ends with exonuclease/polymerase, and the enzymes were then removed. After adenylation of the 3′ ends of the DNA fragments, Illumina PE adapter oligonucleotides were ligated to prepare for hybridization. To select cDNA fragments of the preferred 200 bp in length, the library fragments were purified using the AMPure XP system (Beckman Coulter, Beverly, CA, USA). DNA fragments with ligated adaptor molecules at both ends were selectively enriched with Illumina PCR Primer Cocktail in a 15 cycle PCR. The products were purified in an AMPure XP system and quantified with an Agilent high sensitivity DNA assay on a Bioanalyzer 2100 system (Agilent). The RNA library was then sequenced on the Illumina Hiseq platform by Shanghai Personal Biotechnology Cp. Ltd.

2.10. RNA-Seq analysis

Samples are sequenced on the platform to get image files, which are transformed by the software of the sequencing platform, and the original data in FASTQ format (Raw Data) is generated. Sequencing data contains a number of adapters, low-quality reads, so we use Cutadapt (v1.15) software to filter the sequencing data to get high quality sequence (Clean Data) for further analysis. In data mapping analysis, the reference genome and gene annotation files were downloaded from genome website. Reference genome index was built by Bowtie2 (2.2.6) and the filtered reads were mapping to the reference genome using TopHat2 (2.0.14), the default mismatch was no > 2. The alignment region distribution of mapped reads was calculated. For mRNA analysis, we used HTSEq. (0.9.1) statistics to compare the Read Count values on each gene as the original expression of the gene, and then used FPKM to standardize the expression. Then we used DESEq. (1.30.0) to analyze the genes of difference expression with screened conditions as follows: expression difference multiple |log2 fold change| > 1, significant *p*-value < .05. At the same time, we used R language Pheatmap (1.0.8) software package to perform bi-directional clustering analysis of all different genes of samples. We get heat map according to the expression level of the same gene in different samples and the expression patterns of different genes in the same sample with Euclidean method to calculate the distance and Complete Linkage method to cluster. Next, we mapped all the genes to Terms in the Gene Ontology database and calculated the numbers of differentially enriched genes in each Term. Based on the whole genome, Terms with significant enrichment of differentially enriched genes were calculated by hypergeometric distribution. The purpose of GO enrichment analysis is to obtain GO functional terms with significant enrichment of differentially expressed genes, thus revealing the possible functions of differentially expressed gene in the samples, as well as we counted the number of differentially expressed genes at different levels of KEGG Pathway, and then determined the metabolic pathways and signaling pathways that differentially expressed genes mainly participate in. RNA-seq data has been deposited at: https://dataview.ncbi.nlm.nih.gov/object/PRJNA532295?reviewer=t1qjkmruvftmqoge2eaicj6dut.

2.11. Calcium imaging

Purified astrocyte cell suspensions were transferred to 96-well plates containing DMEM plus 10% fetal bovine serum and cultured to confluence before incubation for 25 min with 1.6 μM Fluo-4 AM (Beyotime Institute of Biotechnology), a fluorescent calcium indicator. The cultures were washed three times with 0.01 M PBS before the culture medium was replaced with DMEM plus 2 μM ethylene glycol-bis (β-aminoethyl ether)-N,N,N′,N′-tetraacetic acid to chelate calcium. Then 1 μM thapsigargin (Tg) was added to induce release of $[Ca^{2+}]_i$. When the $[Ca^{2+}]_i$ was stable, 2 mM $CaCl_2$ solution was added to the DMEM to induce Ca^{2+} influx. The fluorescence intensity was recorded and analyzed with a FlexStation 3 Multi-Mode Microplate Reader (Molecular Devices, Sunnyvale, CA, USA).

2.12. Statistical analysis

All data are presented as the mean ± standard error of the mean. Statistical analyses were performed using Prism software (GraphPad Software, Inc., La Jolla, CA, USA). Data were tested for Gaussian distribution with the Kolmogorov-Smirnov normality test and then analyzed by one-way analysis of variance (ANOVA) and the Dunnett's post hoc test. Statistical significance was set at $p < .05$.

3. Results

3.1. Loss of KCa3.1 expression decreases LPS-induced memory deficiency and neuronal loss

Systemic LPS injection can cause neuroinflammation and memory dysfunction in rats (Song et al., 2016). To test the involvement of KCa3.1 channels in the development of AD-like pathology and symptoms, we administered 8- to 10-week old WT (KCa3.1$^{+/+}$) and KO (KCa3.1$^{-/-}$) mice a single intraperitoneal injection of LPS at 5 mg/kg and tested them in the Morris water maze. The results indicated that knockdown of KCa3.1 expression attenuated the LPS-induced cognitive dysfunction. The WT, KO, WT + LPS, and KO + LPS mice learned to find the hidden platform during a 5-day training period and then were tested for six consecutive days. During the 5-day training period, a spatial learning deficit was observed in WT + LPS mice, as reflected by their requiring more time than the KO + LPS mice to find the hidden platform (Fig. 1A). The KO + LPS mice were resistant to the LPS-induced cognitive dysfunction. After removal of the escape platform, WT + LPS mice performed fewer platform crossings (Fig. 1B), swam shorter distances (Fig. 1C), and spent less time swimming (Fig. 1D) than the KO + LPS mice. Loss of neurons and decrease of synaptic proteins have been found to correlate with AD severity (Pozueta et al., 2013). The immunostaining results indicated that loss of KCa3.1 expression in KO mice prevented neuron loss following LPS injection. NeuN expression was lower in the cortex and CA1 hippocampus in WT + LPS mice than in WT controls (Fig. 1E). NeuN staining was significantly higher in the cortex in KO + LPS mice than in WT + LPS mice. The specificity of the KCa3.1 antibody was shown in the Supplement Fig. 1.

Co-immunostaining of KCa3.1 with specific for GFAP^{+} astrocytes, Iba-1^{+} microglia, and NeuN^{+} neurons was performed on brain sections of control and LPS-stimulated mice (Fig. 1F–H). In control mice, a low level of expression of KCa3.1 was detected in GFAP^{+} astrocytes, Iba-1^{+} microglia, and NeuN^{+} neurons (Fig. 1F–H). However, at LPS-stimulated mice, we detected a clear colocalization between KCa3.1 and GFAP^{+} reactive astrocytes (Fig. 1F). We labeled sections from the LPS groups for KCa3.1 and the Iba1^{+} microglial. There was little colocalization between KCa3.1 and microglia at LPS groups (Fig. 1G). KCa3.1 expression was found in NeuN^{+} neurons in the brains of LPS-stimulated mice (Fig. 1H).

3.2. Loss of KCa3.1 expression decreases LPS-induced glial activation

The results suggested that loss of KCa3.1 in KO mice prevented the activation of microglia activation and reactive astrogliosis that accompany LPS-induced neuroinflammation. Microglial activation by KCa3.1 in LPS-induced mice was investigated by immunostaining of Iba1, which is upregulated in reactive microglia. The immunoreactivity of Iba1 was higher in the cortex and the CA1 and DG hippocampus in the WT + LPS mice than in the WT controls, but was lower in the cortex and hippocampus in KO + LPS mice than in WT + LPS mice (Fig. 2A). The effect of the absence of KCa3.1 on reactive astrocytes in LPS-induced mice was investigated by immunostaining for GFAP. As shown in Fig. 2B, the GFAP immunoreactivity in the hippocampus was higher in WT + LPS mice than in WT controls, but was lower in KO + LPS mice than WT + LPS mice (Fig. 2B). These results suggested that gene deletion of KCa3.1 prevented the microglia activation and reactive astrogliosis in LPS-induced neuroinflammation.

Insulin signaling deficiency may contribute to Tau phosphorylation by modulating Tau kinases, including GSK3β, via the PI3K/AKT signaling pathway (Calvo-Ochoa et al., 2014; Schubert et al., 2004). Western blot assays revealed significantly higher p-Tau expression and significantly lower insulin receptor expression in WT + LPS mice than WT control mice (Fig. 2C). The lack of KCa3.1 in KO mice attenuated the changes in insulin receptor and p-Tau expression in response to LPS. The changes in insulin receptor and p-Tau expression were accompanied by significant decreases in LPS-stimulated phosphorylation of Akt and GSK3β (Fig. 2C), and increases in the phosphorylation of p65 and IκB (Fig. 2C), but these effects were attenuated in KCa3.1-deficient KO mice. Double immunostaining showed that KCa3.1 deficiency attenuated LPS-induced accumulation of insulin and p-Tau in the brain tissue in KO + LPS mice compared with WT + LPS mice (Fig. 2D). A clear colocalization between insulin and NeuN^{+} neuron was detected at LPS-stimulated mice (Fig. 2E).

3.3. Senicapoc inhibits LPS-induced glial activation and neuron loss in vivo

Whether pharmacological blockade of KCa3.1 with senicapoc would attenuate of glial activation and neuron loss in mice treated with LPS was investigated by immunostaining of the astrocytes marker GFAP, microglia marker Iba-1 and neuron marker NeuN. Positive immunostaining of GFAP was significantly increased in the cortex (Fig. 3A, B) in mice treated with LPS compared with control mice, but not in the hippocampus (Fig. 3G, H). Treatment with senicapoc (100 mg/kg, p.o., once daily, 1 h prior to LPS exposure) attenuated GFAP positive immunostaining in the cortex of mice in the LPS + senicapoc group compared with mice in the LPS group (Fig. 3A, B). Positive immunostaining of Iba-1 was also significantly increased in both the cortex (Fig. 3C, D) and hippocampus (Fig. 3I, J) in mice treated with LPS compared with control mice. Treatment with senicapoc attenuated Iba-1 positive immunostaining in the cortex and hippocampus of mice in the LPS + senicapoc group compared with mice in the LPS group.

Immunofluorescence analysis showed that NeuN was decreased in the cortex and hippocampus of LPS mice compared with control mice. Treatment with senicapoc (100 mg/kg, p.o., once daily) led to significantly increased NeuN-positive immunostaining in the cortex (Fig. 3E, F) and hippocampus (Fig. 3K, L) of the LPS + senicapoc group compared with the LPS group.

3.4. KCa3.1 and Orai1 are involved LPS-induced store-operated calcium entry (SOCE) in astrocytes

SOCE channels in the ER are complexes of calcium sensor stromal interaction molecule 1 (STIM1) and pore forming protein calcium release-activated calcium channel protein 1 (Orai1). These channels regulate activation of nonexcitable cells, such as astrocytes and microglia, by triggering Ca^{2+} influx (Gao et al., 2016; Michaelis et al., 2015; Moreno et al., 2012). The activation of KCa3.1 in mast cells depends on Ca^{2+} influx via the Orai1 channel in the plasma membrane (Duffy et al., 2015). We investigated whether Orai1-mediated SOCE might be involved in KCa3.1 activation and the subsequent release of proinflammatory cytokines in LPS-induced astrogliosis. To investigate SOCE transport, we depleted astrocyte ER Ca^{2+} stores with 2 μm Tg, a sarcoplasmic/ER Ca^{2+} ATPase pump blocker. As shown in Fig. 4A, in the absence of extracellular Ca^{2+}, the Tg-evoked increases in [Ca^{2+}]$_i$ (first peak) after 3 h of treatment with 10 μg/ml LPS were no different from those in untreated control astrocytes (Fig. 4A). The addition of 2 mM external Ca^{2+} initiated SOCE within 3 h in LPS-treated cultures. To determine whether LPS-associated SOCE increase might induce Ca^{2+} overload, we blocked KCa3.1 and Orai1 channels with 1 μM senicapoc or 10 μM 2-aminoethoxydiphenyl borate (APB), then measured ER Ca^{2+} release and cellular Ca^{2+} influx after store depletion (Fig. 4A). Blockade of either KCa3.1 or Orai1 abolished astrocyte Ca^{2+} influx

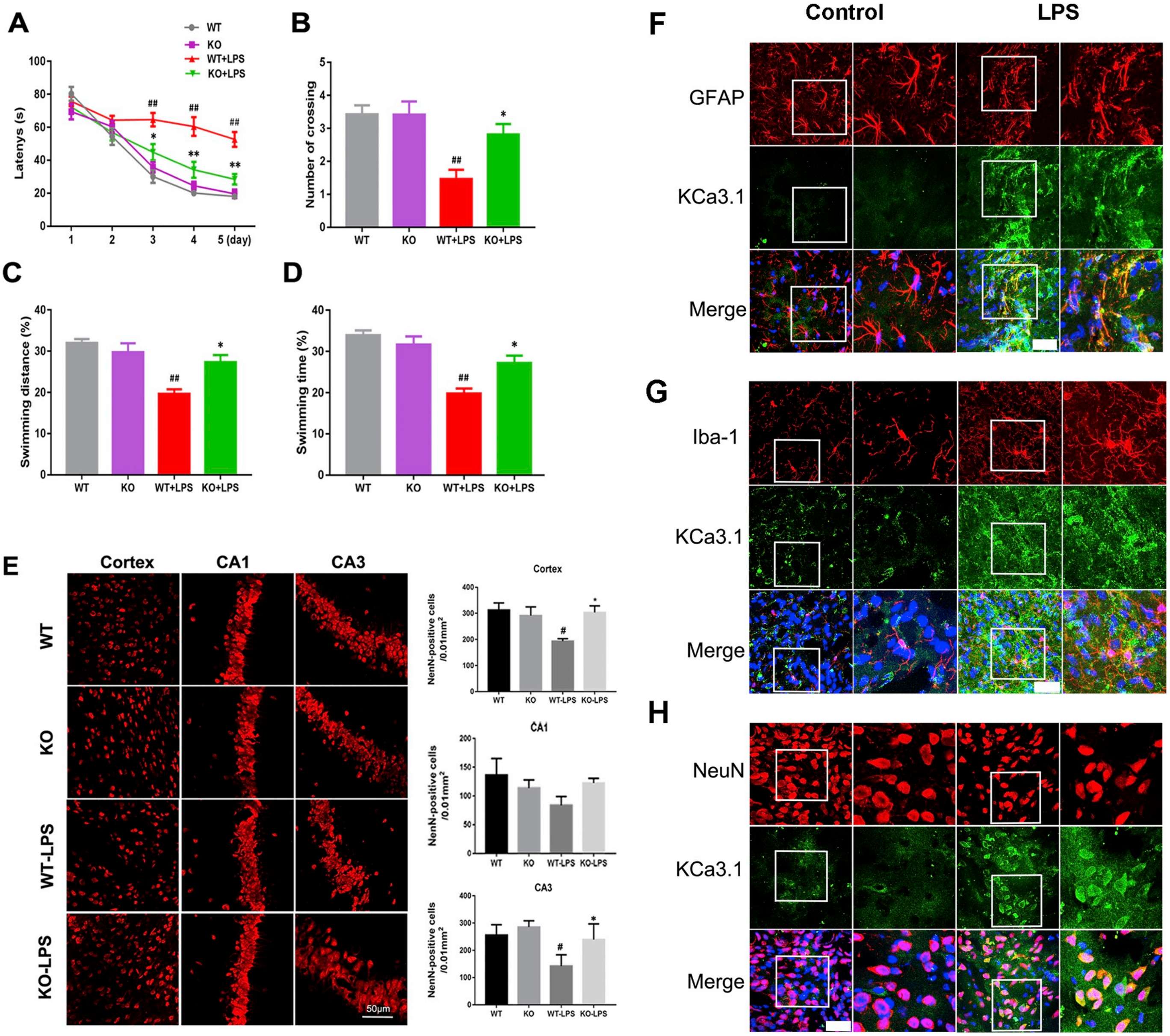

Fig. 1. Gene deletion of KCa3.1 attenuated LPS-induced neuron loss.
KCa3.1 deletion rescued memory deficits after intraperitoneal injection of LPS. The Morris water maze test was performed on WT, KO, WT + LPS and KO + LPS mice as described in the section "Materials and Methods."
(A) Escape latency; (B) Number of crossing the target quadrant by each group during probe trial (no platform); (C) Percentage of swimming distance spent in the target quadrant by each group during probe trial (no platform); (D) Percentage of swimming time spent in the target quadrant by each group during probe trial (no platform). Data represent mean ± SEM (n = 12–16). $^{\#\#}p < .01$ versus WT mice. $^{*}p < .05$, $^{**}p < .01$ versus WT + LPS mice. (E) Cortex and hippocampal CA1 neurons as revealed by NeuN immunohistochemistry. Quantification of neuron number/0.01mm^2 in cortex and hippocampus (n = 6–8). Data represent mean ± SEM. $^{\#}p < .05$ compared with WT mice. $^{*}p < .05$, $^{**}p < .01$ versus WT + LPS group mice. One-way ANOVA followed by the Dunnett's multiple comparison test. WT, wild-type; KO, knockout. Scale bar: 50 μm. F—H, Cellular localization of KCa3.1 channels in mouse brains following LPS stimulation. Double immunofluorescence analysis of KCa3.1 (green) levels in (F) astrocytes (GFAP, red), (G) microglia (Iba-1, red), and (H) neurons (NeuN, red) of control and LPS-stimulated mouse brain. DAPI (blue) was used to label nuclei. Scale bar: 50 μm. (For interpretation of the references to colour in this figure legend, the reader is referred to the web version of this article.)

induced by store depletion, as compared with the response in control cells. Differences in Ca^{2+} transport in WT and KO astrocytes were consistent with KCa3.1 regulation of SOCE in LPS-induced astrocyte activation. $[Ca^{2+}]_i$ was assayed with or without 10 μg/ml LPS for 3 h in WT or KO astrocytes. LPS-induced Ca^{2+} influx was significantly lower in KO than WT + LPS astrocytes (Fig. 4B). The results suggested that KCa3.1 and Orai1 regulate SOCE and cytosolic Ca^{2+} homeostasis in astrocytes and are responsible for Ca^{2+} overload in the promotion of neuroinflammation.

Orai1 was expressed in primary cultures of cortical astrocytes and was found to be associated with LPS-induced TNF-α and IL-6 production. To investigate KCa3.1 activity and the involvement of Orail and SOCE channels in neuroinflammation, we stimulated confluent primary cultures of astrocytes with 10 μg/ml LPS for 1, 3, 5, or 7 days. As shown in Fig. 4, LPS induced a time-dependent upregulation of both KCa3.1 and Orail proteins expression (Fig. 4C, D). The absence of KCa3.1 expression was tested in the brains of KCa3.1 KO mice (Supplement Fig. S2).

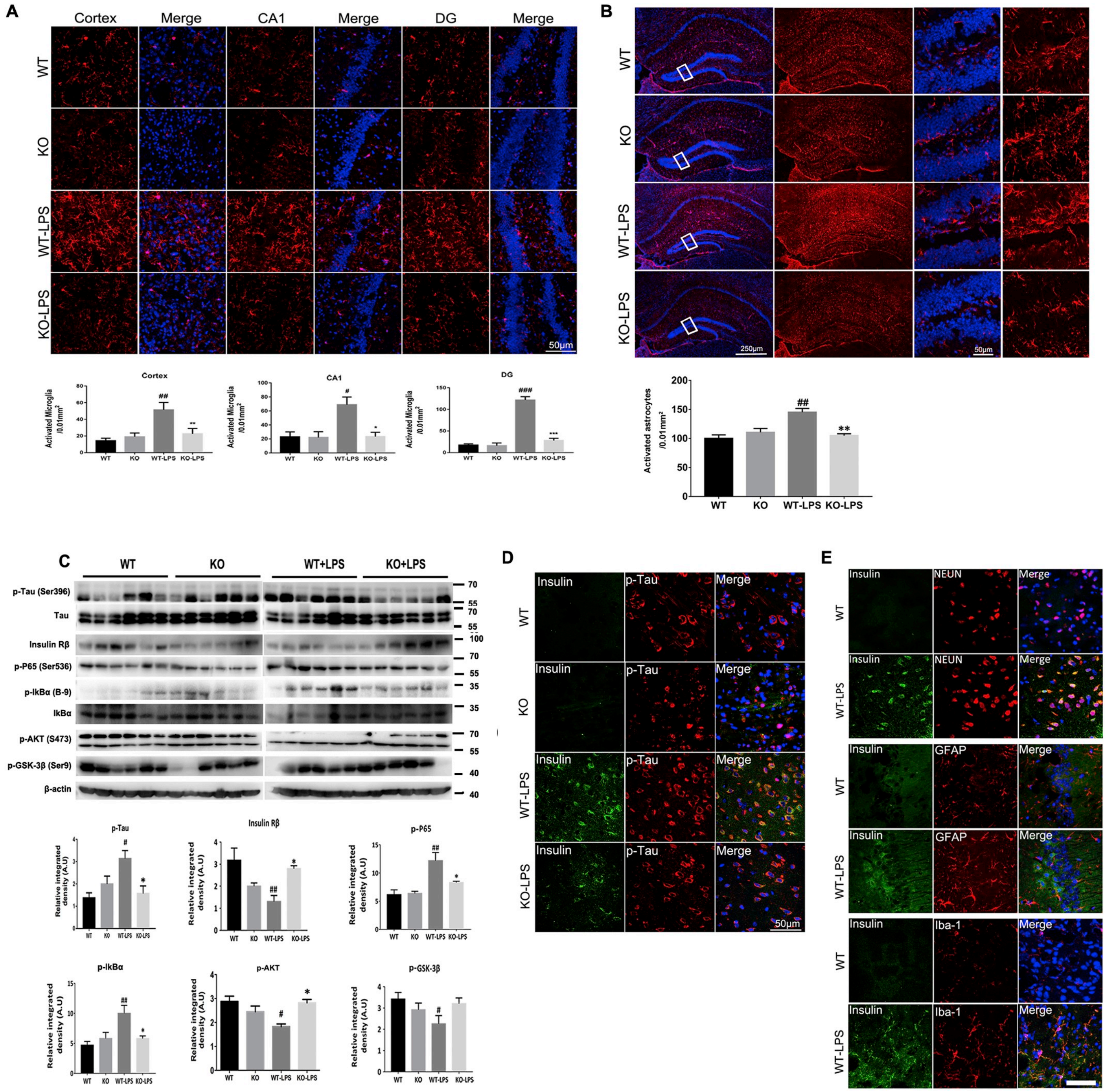

Fig. 2. Gene deletion of KCa3.1 attenuated LPS-induced activated glia.

(A) Representative images of Iba-1-immunoreactive microglia from cortex, hippocampal CA1 and DG regions of WT, KO, WT + LPS and KO + LPS mice. Quantification of activated microglial number/0.01mm^2 in cortex, hippocampal CA1 and DG. Data represent mean ± SEM. $^{\#}p < .05$, $^{\#\#}p < .01$, $^{\#\#\#}p < .001$ compared with WT mice. $^{*}p < .05$, $^{**}p < .01$, $^{***}p < .001$ versus WT + LPS mice ($n = 6$–8). Nuclei were stained blue with DAPI. Scale bar: 50 μm. (B) Representative images of GFAP-immunoreactive astrocytes from hippocampi of WT, KO, WT + LPS and KO + LPS mice. Data represent mean ± SEM. $^{\#\#}p < .01$ compared with WT mice. $^{**}p < .01$ versus WT + LPS mice ($n = 5$). Nuclei were stained blue with DAPI. Scale bar: 250 μm, Scale bar: 50 μm. (C) Western blot analysis of p-Tau, insulin Rβ, p-P65, p-IkBα, p-AKT and p-GSK3β levels in brain homogenates from WT, KO, WT + LPS, and KO + LPS group mice. β-actin was used as the loading control. Data represent mean ± SEM ($n = 6$). $^{\#}p < .05$, $^{\#\#}p < .01$ versus WT mice. $^{*}p < .05$ versus WT + LPS group mice. One-way ANOVA followed by the Dunnett's multiple comparison test. (D) Effect of KCa3.1 deficiency on LPS-induced accumulation of insulin and p-Tau in brain tissues from WT, KO, WT + LPS, and KO + LPS group mice. (E) Cellular localization of insulin in mouse brains following LPS stimulation. Double immunofluorescence analysis of insulin (green) levels in NeuN$^+$ neurons, GFAP$^+$ astrocytes, and Iba-1$^+$ microglia of control and LPS-stimulated mouse brain. DAPI (blue) was used to label nuclei. Scale bar: 50 μm. (For interpretation of the references to colour in this figure legend, the reader is referred to the web version of this article.)

3.5. KCa3.1 is required for LPS-induced reactive astrogliosis and resultant neurotoxicity

We investigated the involvement of KCa3.1 in LPS-induced reactive astrogliosis by pharmacological blockade with the KCa3.1 antagonist senicapoc and in astrocytes from KCa3.1$^{-/-}$ knockout mice. Senicapoc attenuated LPS-induced decreases in astrocyte viability at concentrations of 0.1, 1, 10, and 20 μM in a dose dependent manner (Fig. 5A).

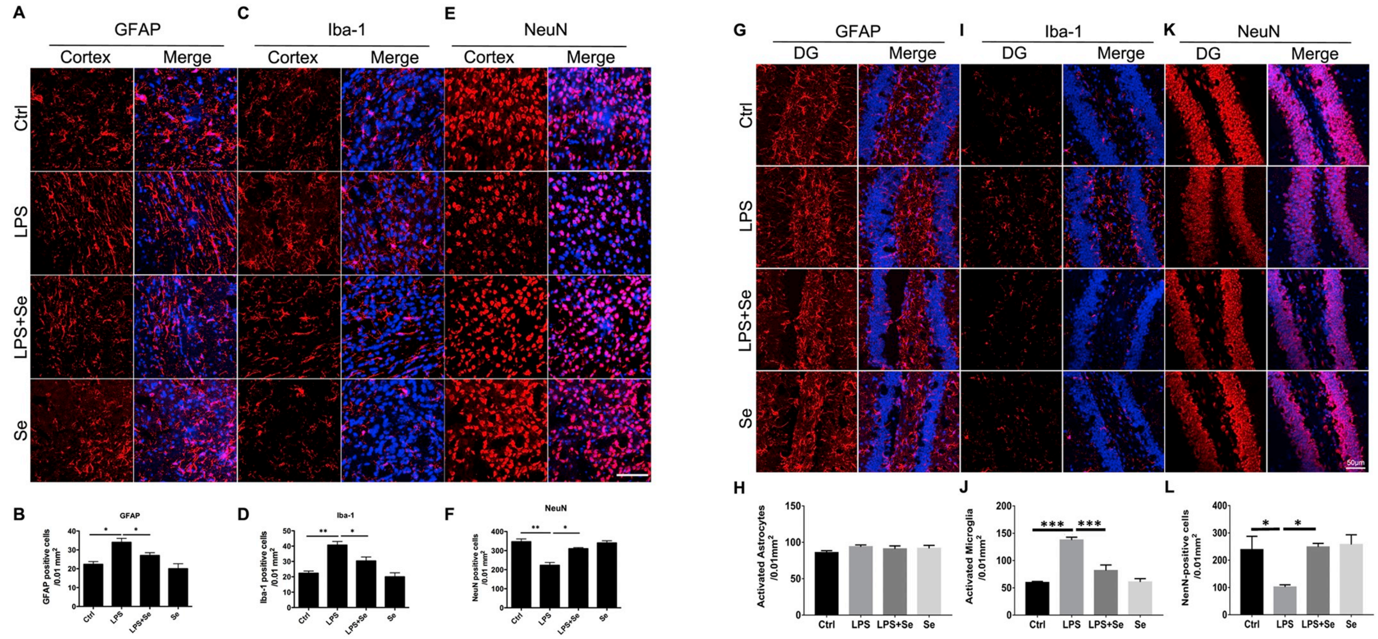

Fig. 3. Senicapoc inhibits LPS-induced glial activation and neuron loss in vivo.

Representative images of (A, G) GFAP$^+$ astrocytes, (C, I) Iba-1$^+$ microglia and (E, K) NeuN$^+$ neuron from cortex (A, C, E) and hippocampus (G, I, K) of control, LPS, LPS + senicapoc and senicapoc mice. Quantification of GFAP$^+$, Iba-1$^+$, and NeuN$^+$ cells/0.01mm^2 in cortex (B, D, F) and hippocampus (H, J, L). Data represent mean ± SEM. $^*p < .05$, $^{**}p < .01$, $^{***}p < .001$. ($n = 6$). Nuclei were stained blue with DAPI. Scale bar: 50 μm. (For interpretation of the references to colour in this figure legend, the reader is referred to the web version of this article.)

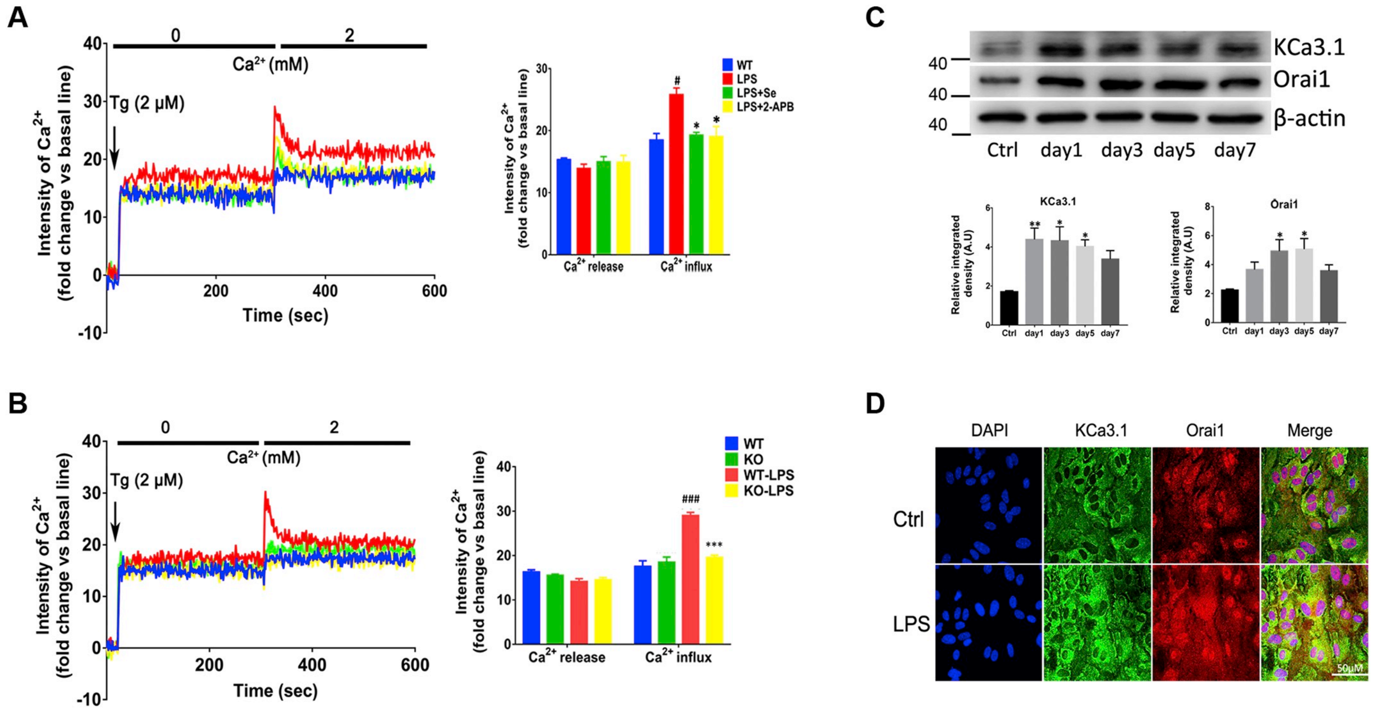

Fig. 4. KCa3.1 involves in LPS-induced SOCE in primary astrocytes.

Astrocytes from WT or KO mice were generated as described in methods and treated for 3 h with 10 μg/ml LPS, labeled with Fluo-4 AM in the absence of LPS (30 min) and rested for 30 min. SOCE was induced by cells stimulation with 2 μM Tg in Ca^{2+}-free culture medium (0 mM Ca^{2+}) followed by addition of 2 mM Ca^{2+}. (A) Calcium influx of astrocytes after treatment with 10 μg/ml LPS for 3 h with or without 1 μM senicapoc or 10 μM 2-APB pretreatment 1 h. $^{\#}p < .05$ versus control cells; $^*p < .05$ versus LPS group cells. (B) Calcium influx of WT or KO astrocytes after treatment with 10 μg/ml LPS for 3 h. $^{\#\#\#}p < .001$ versus WT cells; $^{***}p < .001$ versus WT-LPS group cells. Data represent mean ± SEM ($n = 3$). One-way ANOVA followed by the Dunnett's multiple comparison test. Ctrl, control; Se, senicapoc; WT, wild-type; KO, knockout. (C) Western blot analysis of KCa3.1 and Orai1 expression after 10 μg/ml LPS-treatment for 1, 3, 5, 7 days. Data represent the mean ± SEM of KCa3.1 and Orai1 density normalized to β-actin values for $n = 3$ cultures. $^*p < .05$, $^{**}p < .01$, one-way ANOVA followed by the Dunnett's multiple comparison test compared with control. (D) Double immunofluorescence images of KCa3.1 and Orai1 in cultured astrocytes with or without 10 μg/ml LPS treatment for 3 days. DAPI (blue) was used to label nuclei. Scale bar: 50 μm. (For interpretation of the references to colour in this figure legend, the reader is referred to the web version of this article.)

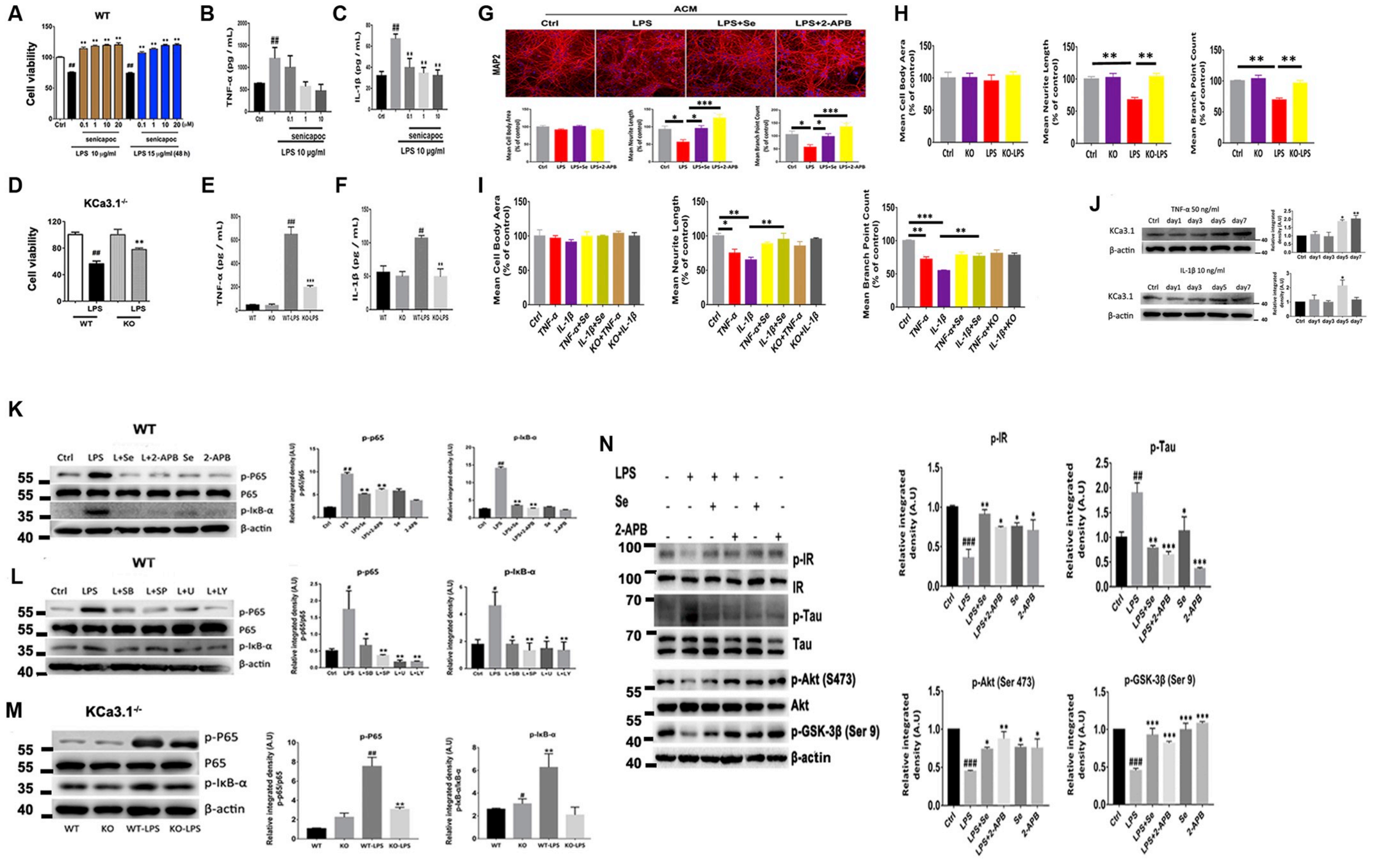

Fig. 5. Effect of senicapoc on LPS-induced phenotype switch of astrocytes and astrogliosis-induced neurotoxicity.
(A) Bar charts showing cell viability of primary astrocytes treated with 10 or 15 μg/ml LPS for 48 h, with or without pretreatment with senicapoc (0.1, 1, 10, 20 μM). Data represent mean ± SEM ($n = 3$). $^{\#\#}p < .01$ versus control cells, $^{**}p < .01$ versus LPS group cells. (B, C) Cytokine TNF-α (B) and Il-1β (C) levels in the medium were measured by ELISA. Data represent mean ± SEM ($n = 3$). $^{\#\#}p < .01$ versus control cells, $^{*}p < .05$, $^{**}p < .01$ versus LPS group cells. (D) Bar charts showing cell viability of WT or KO astrocytes with or without stimulation with 10 μg/ml LPS for 48 h. Data represent mean ± SEM ($n = 3$). $^{\#\#}p < .01$ versus WT cells, $^{**}p < .01$ versus WT + LPS group cells. (E, F) WT or KO astrocytes were stimulated with or without 10 μg/ml LPS for 48 h. Cytokine levels TNF-α (E) and Il-1β (F) in the medium were measured by ELISA. Data represent mean ± SEM ($n = 3$). $^{\#\#}p < .01$, $^{\#\#\#}p < .001$ versus WT cells, $^{**}p < .01$, $^{***}p < .001$ versus WT + LPS group cells. (G-I) Levels of dendritic marker MAP2 were compared between neurons treated with ACM from WT or KO astrocytes with 10 μg/ml LPS, 50 ng/ml TNF-α, or 10 ng/ml IL-1β stimulation for 48 h with or without pretreatment of 1 μM senicapoc or 10 μM 2-APB. Cell body area, neurite length and branch point counts were analyzed by Extended Neurite Outgrowth bioapplication software. Data represent mean ± SEM ($n = 3$). $^{*}p < .05$, $^{**}p < .01$, $^{***}p < .001$ (one-way ANOVA followed by the Dunnett's multiple comparison test). (J) Western blot analysis of KCa3.1 expression after 50 ng/ml TNF-α or 10 ng/ml IL-1β stimulation for 1, 3, 5, 7 days. Data represent mean ± SEM ($n = 3$). $^{*}p < .05$, $^{**}p < .01$ versus control. (K) Western blotting showed the expression of LPS-stimulated p-P65 and p-IκB with the pretreatment of senicapoc or 2-APB. Data represent mean ± SEM ($n = 3$). $^{\#\#}p < .01$ versus control; $^{**}p < .01$ versus LPS group cells. (L) Western blotting showed that compared with the control, p38 MAPK inhibitor SB20358, JNK inhibitor SP600125, ERK inhibitor U0126 and PI3K/AKT inhibitor LY294002 attenuated LPS-induced expression of p-P65 and p-IκB. Data represent mean ± SEM ($n = 3$). $^{\#}p < .05$ versus control; $^{*}p < .05$, $^{**}p < .01$ versus LPS group cells. (M) Western blotting showed the expression of p-P65 and p-IκB in WT and KO astrocytes with LPS stimulation. Data represent mean ± SEM ($n = 3$). $^{\#}p < .05$, $^{\#\#}p < .01$ versus WT; $^{**}p < .01$ versus WT + LPS group cells. (N) Western blotting showed the expression of p-IR, p-Tau, p-AKT and p-GSK3β in LPS-stimulated astrocytes with or without the pretreatment of senicapoc or 2-APB. Data represent mean ± SEM ($n = 3$). $^{\#\#}p < .01$, $^{\#\#\#}p < .001$ versus WT; $^{*}p < .05$, $^{**}p < .01$, $^{***}p < .001$ versus WT + LPS group cells. One-way ANOVA followed by the Dunnett's multiple comparison test.

The effect of LPS on cell viability was inhibited in astrocytes from KCa3.1$^{-/-}$ KO mice, as compared with astrocytes from WT mice (Fig. 5D). The results revealed that KCa3.1 is involved in the LPS-induced inflammatory response of primary astrocytes. Pretreatment with 0.1, 1, or 10 μM senicapoc decreased the TNF-α and IL-1β concentrations in astrocyte culture supernatants after a 48 h exposure to 10 μg/ml LPS (Fig. 5B, C). Increases in LPS-induced TNF-α and IL-1β were attenuated in astrocytes from KO mice compared with those from WT cells (Fig. 5E, F). The effect of senicapoc on cell viability was studied in primary astrocytes (Supplement Fig. S3).

Damage of dendrites and synapses occurs early in AD (Szegedi et al., 2006). We evaluated the regulation of astrogliosis-mediated neurotoxicity by KCa3.1 in mouse neurons cultured in conditioned medium from 10 μg/ml LPS, 50 ng/ml TNF-α, or 10 ng/ml IL-1β stimulated astrocytes (ACM, Fig. 5G–I). Incubation with ACM from LPS, TNF-α, or IL-1β stimulation for 48 h decreased neurite length and branching, but not cell body area, as compared with those in control cultures (Fig. 5G–I). Pharmacological blockade with 1 μM senicapoc (Fig. 5G, I) or gene deletion of KCa3.1 (Fig. 5H, I) significantly reversed the effects of the ACM from LPS, TNF-α, or IL-1β, as shown by an upregulation of neurite length and branching (Fig. 5G–I). As shown in Supplement Fig. S3, the levels of dendritic marker MAP2 were compared between neurons treated with 10 μg/ml LPS for 48 h with or without pretreatment of 1 μM senicapoc (Supplement Fig. S4).

We stimulated confluent primary cultures of astrocytes with 50 ng/ml TNF-α or 10 ng/ml IL-1β for 1, 3, 5, or 7 days. As shown in Fig. 5J, both TNF-α and IL-1β induced a time-dependent upregulation of KCa3.1 proteins expression (Fig. 5J). Together, the results showed that KCa3.1 is indirectly involved in neurotoxicity associated with LPS-induced astrogliosis.

3.6. KCa3.1 and Orai1 are involved in LPS-induced NF-κB activation in astrocytes

As shown in Fig. 5B–F, increased expression of the cytokines IL-1β and TNF-α in response to LPS required activation of the transcription factor NF-κB (nuclear factor kappa-light-chain-enhancer of activated B cells). The results suggested that KCa3.1 and Orai1 mediated the NF-κB activation associated with neuroinflammation. Western blotting analysis confirmed that LPS increased the nuclear translocation of the p65 NF-κB subunit and phosphorylated (p)-IκB and that these effects were attenuated by the KCa3.1 antagonist senicapoc and the Orai1 antagonist 2-APB (Fig. 5K), or deletion of the KCa3.1 gene (Fig. 5M).

The events linking LPS-induced, KCa3.1- and Orai1-mediated Ca^{2+} influx to activation of the NF-κB signaling pathway were investigated with a series of antagonists and pharmacological inhibition experiments. The findings suggested that after LPS exposure, the MAPK and AKT signaling pathways are involved in KCa3.1-mediated NF-κB activation. Western blotting showed that a 30 min exposure of astrocytes to LPS, an ERK inhibitor (10 μM U0126), a JNK inhibitor (10 μM SP600125), a p38 MAPK inhibitor (20 μM SB20358), and a PI3K inhibitor (20 μM LY294002), attenuated LPS-induced upregulation of p65 nuclear translocation and IκB phosphorylation (Fig. 5L).

Insulin resistance leads to Tau hyperphosphorylation by inhibiting AMPK-induced Tau dephosphorylation and promoting aberrant activation of GSK3β through the PI3K/AKT pathway (Kim et al., 2015; Schubert et al., 2004). The results suggest that KCa3.1 promotes accumulation of Tau and insulin signaling deficits during astrogliosis. Western blotting analysis revealed significantly lower expression of insulin receptor and higher expression of p-Tau in LPS-stimulated astrocytes than in controls (Fig. 5N). KCa3.1 blockade with senicapoc or 2-APB attenuated the LPS-induced changes in insulin receptor and p-Tau expression and was accompanied by a significant decrease in Akt phosphorylation and GSK3β activation (Fig. 5N).

3.7. Reactive astrocyte transcriptome expression requires KCa3.1 deficiency

Hierarchical clustering of the LPS-stimulated WT and KO reactive astrocyte populations (Fig. 6A) revealed differences in astrogliosis transcriptomes that corresponded to KCa3.1 status. The transcriptomes included 835 differentially upregulated and 766 differentially downregulated genes with four-fold or greater differences in expression in KO-LPS compared with WT-LPS astrocytes (Fig. 6B); 15,978 genes were common to both types of astrocytes. The 50 upregulated genes with the greatest differences in expression are listed in Table 1. The 50 genes with the greatest degree of downregulation are listed in Table 2. The 20 most enriched Kyoto Encyclopedia of Genes and Genomes (KEGG) pathways in the WT-LPS versus KO-LPS reactive astrocytes are shown in Fig. 6C. The Gene Ontology Consortium classification (http://www.godatabase.org/cgi-bin/amigo/go.cgi) biological process- and class-associated genes with more than four-fold enrichment in WT-LPS and KO-LPS reactive gene sets are shown in Fig. 6D. The most prominent were proteins that function in cell adhesion, phagosomes, neuroactive ligand-receptor interactions, and signaling pathways. The 38 pathways with the most significant enrichment are shown in Table 3. The genes in each of the categories with more than four-fold enrichment in KO-LPS versus WT-LPS reactive astrocytes are listed in Table 4. According to the RNA-seq data (Supplement Fig. S5), LPS can induce A1 phenotype switch in vitro, which was consistent with the previous report in vivo (Liddelow et al., 2017, Nature).

Hierarchical clustering generated a heat map of genes that regulate major histocompatibility complex, cellular adhesion and natural killer cell-mediated cytotoxicity and were found to have significantly increased expression after LPS stimulation for 24 h (Fig. 6E). The bar graph in Fig. 6E shows the average fold change of those genes in WT-LPS and KO-LPS reactive astrocytes. The *H2-D1, H2-Q1*, *H2-BI*, *H2-T10, H2-M2,* and *H2-T3* genes were more strongly induced in WT-LPS reactive astrocytes than KO-LPS cells. Hierarchical clustering showed that the differences in gene expression were partially attributable to variations in WT and KO astrocyte response during LPS-induced cytokine signaling and neuroinflammation (Fig. 6F), but even within that gene classes, differences in induction were clear (Fig. 6F). For example, Il20rb and Ccr1 were increased four-fold; Ccl12 and Ccl19 were increased two-fold; and Cxcr5 and Il13 were increased five-fold.

4. Discussion

Deletion of the gene encoding KCa3.1 decreased the inflammatory response and contributed to attenuation of memory deficits, neuron loss, gliosis, Tau accumulation, and insulin signaling deficits in neuroinflammatory disease. The KCa3.1-induced Tau accumulation and insulin signaling deficits in astrogliosis were both mediated by the PI3K/AKT/GSK3β or NF-κB signaling pathways. KCa3.1 and Orai1 transport contributed to LPS-mediated Ca^{2+} overload and the increased inflammatory response of reactive astrogliosis.

Microglia and astrocytes regulate the severe inflammation that occurs in neurodegenerative diseases (Meraz-Rios et al., 2013; Schilling et al., 2004). Sustained microglial activation and reactive astrogliosis promote chronic dysregulation of glial cells, and subsequent deterioration of brain structure and function (Leszek et al., 2016; Steardo Jr. et al., 2015). Liddelow et al. have reported that A1 reactive astrocytes induced by activated microglia kill neurons and oligodendrocytes. A1 reactive astrocytes are present in human neurodegenerative diseases, including AD and Parkinson's disease. The decreased inflammatory response to LPS demonstrated by astrocytes from KO mice suggested that KCa3.1 is involved in regulating the phenotype switch to astrogliosis in WT astrocytes. KCa3.1 activity was reported to be required for microglial-induced neurotoxicity (Maezawa et al., 2011). We tested the role of KCa3.1 during microglial activation in LPS-induced mice by Iba1 immunostaining in vivo. The Iba1 staining in the cortex and hippocampus of KO + LPS group mice was significantly decreased compared to the WT + LPS group (Fig. 2A). So the genetic deficiency of KCa3.1 reduced LPS-induced memory deficits and neuronal loss, which could also be partly mediated via inhibiting microglia activation. NF-κB activation is known to influence proinflammatory gene expression, and LPS-induced NF-κB activation was lower in KCa3.1-deficient than in WT astrocytes. According to our RNA-seq data (Supplement Fig. S5), LPS can induce A1 phenotype switch in vitro, which was consistent with the previous report in vivo (Liddelow et al., 2017, Nature). As shown in Fig. 5, gene deletion or pharmacological blockade of KCa3.1 attenuated the TNF-α and IL-1β concentrations in astrocyte culture supernatants, thus resulting in attenuating the synapses injury during neuroinflammation.

Transient increases in $[Ca^{2+}]_i$ result in prolonged approximately 60% site-selective increases in tau phosphorylation at the Tau-1 epitope via a glycogen synthase kinase 3 beta (GSK-3β)-dependent pathway (Hartigan and Johnson, 1999). Calcineurin, Ca^{2+}/calmodulin dependent protein phosphatase, is reported to have a link between dysregulation of Ca^{2+} and the astrocyte phenotype switch. Calcineurin-dependent transcription factor nuclear factor of activated T cells (NFAT) is also upregulated in reactive astrogliosis in neurodegeneration disease mice models. Calcineurin/NFAT signal pathway hyperactivation of reactive astrogliosis is involved in the process of neuroinflammation and synapse dysfunction (Sompol and Norris, 2018).

Ca^{2+} mobilization from astrocyte ER stores is key in brain functioning. For example, regenerative opening of ER Ca^{2+} channels increases astrocyte $[Ca^{2+}]_i$, which in turn regulates neuronal plasticity (Khakh and McCarthy, 2015; Newman, 2015). The channels that regulate SOCE and thus maintain Ca^{2+} homeostasis in astrocytes are unclear. The SOCE channels that regulate Ca^{2+} influx in nonexcitatory cells such as astrocytes and microglia include an ER calcium sensor (STIM) and a pore protein (Orai1). The STIM1 and Orai1 proteins have been identified in primary cultured cortical astrocytes, and SOCE is

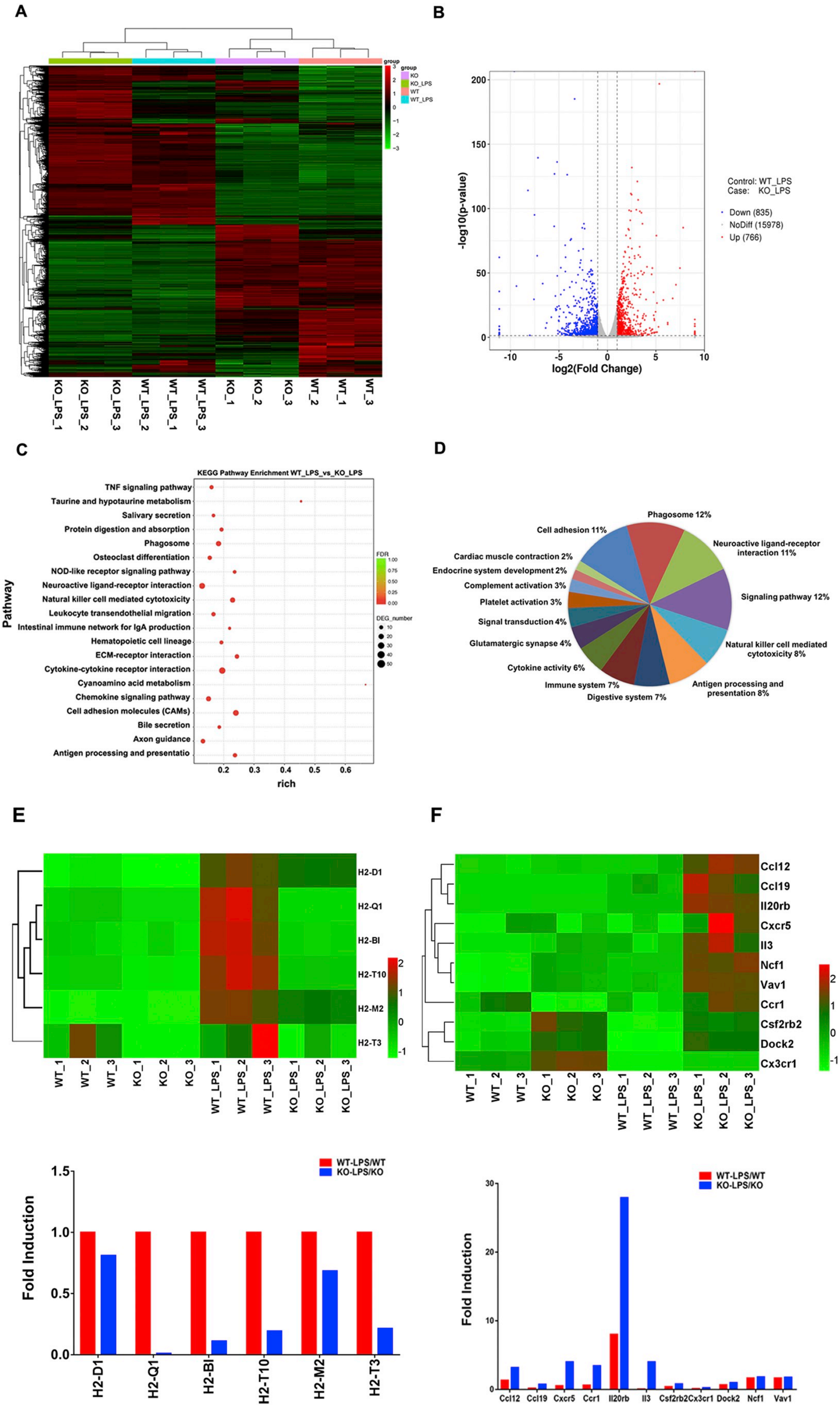

(caption on next page)

Fig. 6. LPS-induced phenotype switch of reactive astrocytes with KCa3.1 deficiency has overlapping but distinct sets of induced genes.
A, A heat map was generated by hierarchical clustering using the relative expression of each probe set is indicated by colour intensity, where green indicates lower expression and red indicates higher expression in 24 h LPS-treated WT and KO astrogliosis. B, Volcano map shows the 17579 genes expressed in WT-LPS and KO-LPS, the abscissa is log2 Fold Change and the ordinate is -log10 (*p*-value). The two vertical dotted lines in the figure are the two-fold difference threshold; the horizontal dotted line is the threshold, *p*-value = .05. (red, increase; blue, decrease; gray, no change). Differential expression analysis comparing WT-LPS and KO-LPS reactive astrocytes identified the 835 genes significantly upregulated and 766 genes significantly downregulated compared with the WT-LPS reactive astrocytes. 15978 genes are common to both types of reactive astrocytes. C, The KEGG Pathway Enrichment shows the top 20 pathways that enriched in WT-LPS vs KO-LPS reactive astrocytes. D, Pie charts show the Gene Ontology categorization of WT-LPS and KO-LPS reactive gene sets. Cell adhesion, phagosome, neuroactive ligand-receptor interaction and signaling pathway are prominent classes. E, A heat map was generated by hierarchical clustering using major histocompatibility complex/cellular adhesion/natural killer cell-mediated cytotoxicity genes whose expression was significantly induced after 24 h LPS stimulation. (red, increase; blue, decrease; gray, no change). The bar graph shows the fold induction of genes within the class in WT-LPS reactive astrocytes (red) and KO-LPS reactive astrocytes (blue). All replicates within a class were averaged to obtain the fold induction. Major histocompatibility complex/cellular adhesion/natural killer cell-mediated cytotoxicity genes *H2-D1, H2-Q1*, *H2-BI*, *H2-T10, H2-M2,* and *H2-T3* are more strongly induced in WT-LPS reactive astrocytes than KO-LPS cells. F, A heat map was generated by hierarchical clustering of resting and reactive astrogliosis populations using cytokine signaling genes whose expression is significantly induced after 24 h LPS stimulation in both WT and KO cells. (red, increase; blue, decrease; gray, no change). The bar graph shows fold induction of cytokine signaling genes in WT-LPS reactive astrocytes (red) and KO-LPS reactive astrocytes (blue). All replicates within a class were averaged to obtain the fold induction. The cytokines *Csf2rb2, Cx3cr1, Dock2, Ncf1, and Vav1* are similarly induced in both WT-LPS and KO-LPS reactive astrocytes. The cytokines *Ccl12, Ccl19, Cxcr5, Ccr1, Il20rb, and Il13* are more strongly induced in KO-LPS reactive astrocytes. (For interpretation of the references to colour in this figure legend, the reader is referred to the web version of this article.)

Table 1
Top 50 upregulated genes in KO-LPS vs. WT-LPS reactive astrocytes.

ID	Name	WT-LPS	KO-LPS	Fold change
ENSMUSG00000066258	Trim12a	4.7	2413.5	517.1
ENSMUSG00000037849	Ifi206	1.0	217.0	225.1
ENSMUSG00000073491	Ifi213	0.7	124.1	178.8
ENSMUSG00000092277	Gm19684	0.7	93.2	134.3
ENSMUSG00000003484	Cyp4f18	0.6	68.8	106.5
ENSMUSG00000078810	Gp6	0.3	25.4	74.4
ENSMUSG00000036594	H2-Aa	0.3	22.7	74.4
ENSMUSG00000056306	Sertm1	1.3	70.6	54.6
ENSMUSG00000067212	H2-T23	140.6	5749.0	40.9
ENSMUSG00000078452	Raet1d	1.0	38.6	38.6
ENSMUSG00000030737	Slco2b1	0.4	12.3	34.8
ENSMUSG00000027219	Slc28a2	2.0	69.3	34.5
ENSMUSG00000079597	Gm5483	7.5	247.4	33.2
ENSMUSG00000043939	A530064D06Rik	0.3	9.7	31.7
ENSMUSG00000045868	Gvin1	2.1	65.9	31.3
ENSMUSG00000002324	Rec8	1.6	46.5	28.9
ENSMUSG00000031803	B3gnt3	1.3	37.4	28.4
ENSMUSG00000058626	Capn11	0.3	8.6	28.3
ENSMUSG00000043036	Ccdc63	0.3	8.6	28.3
ENSMUSG00000094733	Gm5416	0.3	9.6	28.2
ENSMUSG00000034987	Hrh2	1.7	45.3	27.3
ENSMUSG00000041782	Lad1	3.7	99.3	27.2
ENSMUSG00000069733	Ube2u	0.7	16.4	25.0
ENSMUSG00000054905	Stfa3	17.1	424.8	24.8
ENSMUSG00000078496	Zfp982	0.4	8.7	24.7
ENSMUSG00000062310	Glrp1	0.6	15.7	24.3
ENSMUSG00000053338	Tarm1	6.4	151.5	23.6
ENSMUSG00000092074	Dynlt1a	0.3	8.0	23.4
ENSMUSG00000071112	Spx	0.6	13.6	22.3
ENSMUSG00000026343	Gpr39	1.0	19.6	20.6
ENSMUSG00000022803	Popdc2	0.3	6.0	19.8
ENSMUSG00000039209	Rpl39l	0.3	5.7	18.6
ENSMUSG00000050640	Tmem150c	0.3	6.0	17.6
ENSMUSG00000006154	Eps8l1	11.6	197.0	16.9
ENSMUSG00000078902	Gm14443	1.1	17.0	16.1
ENSMUSG00000039155	Cdh26	6.1	96.1	15.8
ENSMUSG00000043289	Mei4	3.3	51.7	15.6
ENSMUSG00000049848	Ceacam19	1.0	15.7	15.5
ENSMUSG00000055826	Tescl	0.7	10.0	15.2
ENSMUSG00000102418	Sh2d1b1	0.6	9.4	14.5
ENSMUSG00000056054	S100a8	23.2	333.0	14.3
ENSMUSG00000058818	Pirb	29.6	406.3	13.7
ENSMUSG00000079547	H2-DMb1	5.1	69.5	13.7
ENSMUSG00000030670	Cyp2r1	1.0	13.7	13.5
ENSMUSG00000030154	Klrb1f	0.6	8.3	12.9
ENSMUSG00000048617	Rtbdn	0.3	4.4	12.9
ENSMUSG00000058246	Gm10037	4.4	55.8	12.8
ENSMUSG00000026414	Tnnt2	4.0	50.3	12.6
ENSMUSG00000029370	Rassf6	15.7	194.8	12.4

Shown are the top 50 genes in order of fold change with normalized linear expression in LPS astrocytes.

Table 2
Top 50 downregulated genes in KO-LPS vs. WT-LPS reactive astrocytes.

ID	Name	WT-LPS	KO-LPS	Fold change
ENSMUSG00000026535	Ifi202b	3818.7	1.7	2278.6
ENSMUSG00000058126	Tpm3-rs7	1553.6	2.0	776.6
ENSMUSG00000040264	Gbp2b	1570.1	2.4	666.3
ENSMUSG00000039146	Ifi44l	297.2	1.0	293.2
ENSMUSG00000066000	Zfp979	261.1	1.0	257.2
ENSMUSG00000070713	Gm10282	64.5	0.3	191.0
ENSMUSG00000057503	Olfr1459	243.0	1.3	183.5
ENSMUSG00000096528	G430049J08Rik	151.5	1.0	151.3
ENSMUSG00000059040	Eno1b	999.9	7.0	143.3
ENSMUSG00000079507	H2-Q1	136.9	1.3	102.1
ENSMUSG00000067608	Pcna-ps2	55.8	0.7	82.6
ENSMUSG00000051111	Sv2c	24.9	0.3	76.6
ENSMUSG00000049154	Fam183b	36.5	0.7	55.1
ENSMUSG00000030329	Pianp	257.3	5.7	45.0
ENSMUSG00000035683	Melk	439.8	10.0	44.0
ENSMUSG00000113061	Gm11361	82.5	2.0	41.2
ENSMUSG00000012123	Crybg2	55.0	1.4	40.6
ENSMUSG00000025347	Mettl7b	52.4	1.3	39.6
ENSMUSG00000024261	Syt4	101.9	2.7	38.3
ENSMUSG00000028610	Dmrtb1	60.7	1.7	36.5
ENSMUSG00000101523	Gm10031	517.8	14.2	36.4
ENSMUSG00000091900	Gm4353	132.2	3.7	35.9
ENSMUSG00000043424	Eif3j2	220.1	6.4	34.6
ENSMUSG00000048070	Pirt	11.1	0.3	34.3
ENSMUSG00000048065	Cyb5r2	33.1	1.0	32.6
ENSMUSG00000052229	Gpr17	64.0	2.0	32.0
ENSMUSG00000096141	Dnah7a	31.5	1.0	31.9
ENSMUSG00000073876	Gm13305	41.4	1.3	31.2
ENSMUSG00000045318	Adra2c	10.5	0.3	31.0
ENSMUSG00000032889	Gm6685	10.1	0.3	29.7
ENSMUSG00000079492	Gm11127	58.8	2.0	29.6
ENSMUSG00000013523	Bcas1	93.3	3.3	28.0
ENSMUSG00000027014	Cwc22	19052.4	681.0	28.0
ENSMUSG00000048038	Ccdc187	8.9	0.3	26.3
ENSMUSG00000051076	Vtcn1	8.5	0.3	26.1
ENSMUSG00000048304	Slitrk3	17.6	0.7	26.0
ENSMUSG00000072066	6720489N17Rik	222.9	8.7	25.5
ENSMUSG00000047976	Kcna1	17.2	0.7	25.4
ENSMUSG00000049583	Grm5	42.0	1.7	25.1
ENSMUSG00000050272	Dscam	54.2	2.4	22.8
ENSMUSG00000079364	Gm3558	7.6	0.3	22.5
ENSMUSG00000032854	Ugt8a	29.6	1.3	22.2
ENSMUSG00000010505	Myt1	111.2	5.0	22.2
ENSMUSG00000044681	Cnpy1	13.8	0.7	20.8
ENSMUSG00000044103	Il1f9	260.1	12.7	20.5
ENSMUSG00000021789	Sftpa1	6.9	0.3	20.4
ENSMUSG00000061062	Gm10093	168.8	8.3	20.2
ENSMUSG00000022441	Efcab6	6.8	0.3	20.1
ENSMUSG00000037686	Aspg	511.1	25.7	19.9
ENSMUSG00000036853	Mcoln3	6.7	0.3	19.8

Shown are the top 50 genes in order of fold change with normalized linear expression in LPS astrocytes.

Table 3
Enrichment analysis of pathways induced in KO-LPS vs WT-LPS reactive astrocytes.

Pathways	*p* Value	Genes
Cell adhesion molecules (CAMs)	1.20E-10	Itgb2 Itgb7 Madcam1 H2-M10.2 Itga4 Siglec1 Itgam Itgal Cdh5 H2-Aa F11r H2-T24 H2-T22 H2-Q7 H2-K1 H2-T23 H2-Q10 H2-Ab1 H2-DMb1 Nrxn3 Nrcam Spn H2-Q1 Ocln Ncam2 H2-T10 H2-Bl Cldn23 L1cam Sele Cldn1 Cldn2 Cntn1 Cdh1 Cldn10 Gm11127 H2-T3 Vtcn1
Cytokine-cytokine receptor interaction	4.63E-10	Tnfsf10 Osm Ccl12 Cxcl3 Ccl19 Cxcl9 Il15 Il10 Cxcl14 Il23r Csf1r Ccl4 Cxcr5 Cd70 Ccr1 Tnfrsf1b Tnfrsf11a Cxcl10 Il21r Tnfrsf8 l20rb Tnfsf13b Il3 Ccl5 Csf2rb2 Ccl27a Ccl3 Csf3 Csf2ra lIl10ra Tnfsf9 Tnf Cx3cr1 Csf2rb Cxcl11 Bmp7 Tnfsf18 Il6ra Tslp Lta Pdgfra Ccl20 Edar Kitl Tgfb2 Gm20878 Cxcl1 Ccr5 Tnfsf8 Gm13305
Natural killer cell mediated cytotoxicity	1.98E-08	H2-M10.2 Tnfsf10 Rac3 Lcp2 Fcer1g Sh2d1b1 H2-Q10 Tyrobp H2-T22 H2-K1 Ptpn6 H2-Q7 Cd48 Cd244 Itgb2 Rac2 Ptk2b Raet1d Vav1 Tnf Itgal Fcgr4 H2-T23 H2-T24 H2-Q1 Shc4 H2-T10 H2-Bl Raet1e H2-T3 Gm11127
ECM-receptor interaction	2.36E-06	Itga2 Itgb7 Col6a4 Col1a2 Col2a1 Gp6 Spp1 Itga4 Reln Tnr Hmmr Col6a2 Lama3 Itga11 Lama1 Col4a3 Sv2c Sv2b Itga7 Col6a5
Phagosome	3.75E-06	Itga2 H2-M10.2 Msr1 Ctss Tubb3 H2-Q10 H2-T22 Coro1a Clec7a H2-K1 H2-Aa Fcgr1 H2-Q7 Fcgr2b Itgb2 H2-Ab1 Ncf2 Itgam Ncf1 Fcgr4 H2-DMb1 H2-T23 H2-T24 C1rb H2-Q1 H2-Bl H2-T10 Pla2r1 Sftpa1 Gm11127 H2-T3
Antigen processing and presentation	6.39E-06	H2-M10.2 Hspa1l Ctss H2-Ab1 Tnf Hspa1b H2-Q10 H2-T22 H2-K1 H2-Aa H2-DMb1 H2-Q7 H2-T24 H2-T23 H2-Q1 H2-T10 H2-Bl H2-T3 Gm11127
NOD-like receptor signaling pathway	1.92E-04	Naip2 Naip6 Pycard Ccl12 Nod1 Nod2 Ccl5 Pstpip1 Nlrp1a Tnf Card9 Naip5 Nlrp3
Protein digestion and absorption	2.99E-04	Prcp Kcnn4 Atp1a3 Slc7a8 Col6a4 Col22a1 Fxyd2 Col1a2 Col2a1Col27a1 Slc1a1 Col4a3 Col6a2 Slc1a5 Col24a1 Col6a5 Col11a2
Chemokine signaling pathway	3.90E-04	Adcy7 Ccl12 Cxcl3 Ccl19 Ccl5 Cxcl9 Was Ccl27a Ccl3 Rac2 Cxcl14 Ptk2b Ccl4 Dock2 Cxcr5 Vav1 Ncf1 Cx3cr1 Ccr1 Cxcl10 Cxcl11 Ccl20 Adcy1 Shc4 Plcb2 Gm20878 Cxcl1 Ccr5
Cyanoamino acid metabolism	4.43E-04	Ggt5 Ggt1 Ggt6 Shmt2
Hematopoietic cell lineage	4.57E-04	Itga2 Cd33 Csf2ra Il3 Csf1r Cd37 Itgam Cd5 Tnf Csf3 Fcgr1 Itga4 Il6ra Cd59a Gm13305 Kitl
Neuroactive ligand-receptor interaction	6.55E-04	Cnr2 Gpr156 Lpar2 Adora3 C3ar1 Adora2a Fpr1 Grid1 Grm7 Grm8 Ltb4r2 Hrh2 Grin3a Grid2 Grik3 Gipr Chrna4 Gabbr2 Gria1 Gria2 Grik4 Sctr P2ry14 Ntsr2 Gabrb3 Nts Grik1 Trhr Gal Gabrg1 Gabra2 Agtr2 Grm5 Npy6r Lpar4 Adra2c Ptger3 Glp1r F2rl1 Gabra4
Taurine and hypotaurine metabolism	7.94E-04	Ggt5 Ggt1 Ggt6 Cdo1 Gad1
Leukocyte transendothelial migration	9.42E-04	Itgb2 Ptk2b Rac2 Cdh5 Itgam Card9 Mmp2 Vav1 Itgal Ncf1 Ctnna2 F11r Itga4 Mmp9 Ocln Cldn10 Cldn1 Cldn23 Cldn2
Bile secretion	2.16E-03	Slco1a6 Slco1a4 Abcb4 Adcy7 Atp1a3 Slco1a5 Fxyd2 Aqp1 Abcb1b Slc5a1 Sctr Adcy1 Kcnn2
Osteoclast differentiation	2.36E-03	Ctsk Lcp2 Tyrobp Spi1 Lilra5 Fcgr1 Fcgr2b Trem2 Csf1r Ncf2 Tnf Pirb Ncf1 Tnfrsf11a Fcgr4 Blnk Tgfb2 Acp5
TNF signaling pathway	2.61E-03	Ccl12 Creb3l4 Cxcl3 Nod2 Ccl5 Tnf Mmp14 Il15 Ptgs2 Tnfrsf1b Cxcl10 Cebpb Mmp9 Ccl20 Lta Sele Cxcl1
Intestinal immune network for IgA production	3.16E-03	Itgb7 H2-Ab1 Tnfsf13b Il15 H2-Aa Il10 H2-DMb1 Madcam1 Itga4
Salivary secretion	5.72E-03	Fxyd2 Lyz2 Adcy7 Kcnn4 Atp1a3
Axon guidance	6.63E-03	Robo3 Pdk1 Rac2 Rac3 Ablim1 Ephb1 Fes Sema4d Plxnb3 Shh Bmp7 L1cam Sema4f Sema3e Ngef Ptch1 Wnt4 Trpc6 Dcc Sema5a Sema3d Plxna4 Trpc3
Mineral absorption	6.89E-03	Fxyd2 Hmox1 Atp1a3 Slc40a1 Slc11a1 Vdr Slc5a1 Trpm6
Methane metabolism	1.70E-02	Glyctk Eno1b Psat1 Fbp2 Shmt2 Fbp1
Regulation of lipolysis in adipocytes	2.21E-02	Ptgs1 Ptgs2 Adcy7 Fabp4 Npy Adcy1 Irs4 Ptger3 Prkg2
cAMP signaling pathway	2.38E-02	Tnni3 Adcy7 Rac2 Rac3 Atp1a3 Creb3l4 Vav1 Fxyd2 Adora2a Npy Hcar2 Grin3a Calml4 Gli1 Adcy1 Gipr Gabbr2 Ptch1 Gria1 Gria2 Atp2b4 Ptger3 Glp1r
Glutamatergic synapse	2.43E-02	Pla2g4b Adcy7 Grm7 Grm8 Grin3a Grik3 Slc1a1 Adcy1 Grm5 Plcb2 Gria1 Gria2 Grik4 Slc17a8 Grik1
Hedgehog signaling pathway	3.04E-02	Ptch2 Shh Gli1 Wnt7b Ptch1 Wnt4 Lrp2 Cdon
Carbon fixation in photosynthetic organisms	3.20E-02	Gapdh Fbp2 Tktl1 Fbp1
Platelet activation	3.65E-02	Itga2 Pla2g4b Adcy7 Lcp2 Fcer1g Ptgs1 P2ry12 Col1a2 Gp6 Fermt3 Fermt3 Adcy1 Plcb2 Prkg2 Gucy1b1
Phospholipase D signaling pathway	3.95E-02	Pla2g4b Ptk2b Adcy7 Cyth4 Lpar2 Fcer1g Dnm3 Grm7 Grm8 Pdgfra Adcy1 Grm5 Shc4 Plcb2 Lpar4 Kitl Pip5k1b
Cardiac muscle contraction	4.18E-02	Fxyd2 Tnnt2 Tpm3 Tnni3 Cox6b2 Atp1a3 Cox7a2l Cacng4 Cacna2d3 Cox6a2
Focal adhesion	4.50E-02	Itga2 Itgb7 Rac2 Rac3 Vav1 Col6a4 Col2a1 Col1a2 Spp1 Itga4 Reln Tnr Pdgfra Shc4 Col6a2 Rasgrf1 Lama3 Lama1 Itga11 Col4a3 Itga7 Col6a5
Fc epsilon RI signaling pathway	5.23E-02	Pla2g4b Inpp5d Rac2 Rac3 Il3 Vav1 Lcp2 Fcer1g Tnf
Pentose and glucuronate interconversions	5.25E-02	Akr1b8 Dcxr Ugt1a7c Gusb Ugt1a6b Ugt2b5
Mucin type O-Glycan biosynthesis	5.76E-02	Galnt12 Gcnt1 Galnt6 Galnt15 Galnt16
Rap1 signaling pathway	6.71E-02	Itgb2 Adcy7 Rac2 Rac3 Csf1r Itgam Lcp2 Lpar2 Fgf1 Itgal Adora2a Fpr1 Calml4 Pdgfra Adcy1 Plcb2 Lpar4 Kitl Ngf Angpt4 Cdh1 Fgf10
PI3K-Akt signaling pathway	6.71E-02	Ccl12 Creb3l4 Cxcl3 Nod2 Ccl5 Tnf Mmp14 Il15 Tnfrsf1b Cxcl10 Cebpb Mmp9 Ccl20 Lta Sele Cxcl1
Complement and coagulation cascades	7.00E-02	Procr C1qb Itgb2 C3ar1 A2m Itgam Cfi Masp2 Cd46 C1rb Cd59a

Shown are the top 38 pathways identified using enrichment analysis of pathways of genes enriched in LPS reactive astrocytes.

involved in LPS-induced production of the cytokines TNF-α and IL-6 in astrocytes. The KCa3.1 channel and Orai1 protein in the human lung mast cell plasma membrane have been reported to mediate SOCE. Ca^{2+}-bound calmodulin was also reported to bind to the core region of activated STIM1, which involved in slowing Ca^{2+}-dependent inactivation after STIM1-induced the activation of Orai1 channel. The calmodulin binding site on STIM1 is close to the STIM1/Orai1 coupling region. The binding of calmodulin to activated STIM1 disrupts both the STIM1/Orai1 complex and the STIM1 oligomer, thereby inducing deactivation of the SOCE (Li et al., 2017).

Senicapoc (ICA-17043) is a selective KCa3.1 inhibitor with an IC_{50} of 11 nM in the sickle cell anemia model in which it was first described (Ataga et al., 2006; Stocker et al., 2003). More recently, (Staal et al., 2017) reported that senicapoc attenuates peripheral nerve injury in a rat model and inhibits the KCa3.1 channel in rat microglia. Another KCa3.1 inhibitor, TRAM-34, has been found to block the release of reactive oxygen species and IL-1β in microglia (Kaushal et al., 2007; Khanna et al., 2001). Senicapoc may be more useful than TRAM-34 as a KCa3.1 blocker in studies of neurodegenerative disease models because it has several fold higher brain concentrations in the brain.

Neuronal circuits involved in glucose sensing in the CNS have been described, but the involvement of glial cells is unclear and central insulin signaling may be involved in regulating systemic glucose metabolism. Ablation of astrocyte insulin receptors has been shown to affect cellular morphology, circuit connectivity, and mitochondrial function (Zakaria et al., 2016). The molecular mechanisms of the insulin signaling deficit that occurs in AD pathogenesis are unclear, but Tau hyperphosphorylation has been found to induce oligomeric insulin accumulation and insulin resistance in neurons (Rodriguez-Rodriguez et al., 2017). Insulin retention causes insulin resistance in

Table 4
Groupings of induced genes based on GO enrichment and KEGG enrichment.

GO enrichment grouping	Genes
Cell adhesion	Itgb7 Itgam H2-Aa H2-T24 H2-T22 H2-K1 H2-T23 H2-Ab1 H2-DMb1 H2-Q1 H2-T10 H2-Bl Cntn1 Cdh1 Cldn10 Gm11127 H2-T3v Vtcn1
Cytokine activity	Ccl19 Cxcr5 Il20rb Il3 Csf2rb2 Cx3cr1 Tslp Kitl Gm13305
Ntural killer cell mediated cytotoxicity	Fcer1g Sh2d1b1 H2-T22 H2-K1 Raet1d H2-T23 H2-T24 H2-Q1 H2-T10 H2-Bl H2-T3 Gm11127
Phagosome	Itga2 Tubb3 H2-T22 H2-K1 H2-Aa Fcgr1 Fcgr2b H2-Ab1 C1rb H2-Q1 H2-Bl H2-T10 Sftpa1 Gm11127 H2-T3 H2-DMb1 H2-T23 H2-T24
Antigen processing and presentation	Hspa1l H2-Ab1 H2-T22 H2-K1 H2-Aa H2-DMb1 H2-T24 H2-T23 H2-Q1 H2-T10 H2-Bl H2-T3 Gm11127
Digestive system	Slco1a6 Abcb4 Slco1a5 Fxyd2 Slc5a1 Sctr Kcnn4 Col6a4 Fxyd2 Slc1a1 Col6a5
Immune system	Il3 Fcgr1 Cd59a Gm13305 Kitl Cnr2 Cldn10 Itgb7 H2-Ab1 H2-Aa H2-DMb1
Neuroactive ligand-receptor interaction	Grm8 Ltb4r2 Hrh2 Grik3 Gipr Chrna4 Sctr Trhr Gal Gabrg1 Gabra2 Grm5 Npy6r Adra2c Ptger3 Glp1r Gabra4
Endocrine system development	Irs4 Ptger3 Prkg2
Signal transduction	Fxyd2 Calml4 Gli1 Gipr Ptger3 Glp1r
Glutamatergic synapse	Pla2g4b Grm8 Grik3 Slc1a1 Grm5 Slc17a8 Grik1
Platelet activation	Pla2g4b Fcer1g Gp6 Prkg2 Gucy1b1
Signaling pathway	Calml4 Pdgfra Kitl Angpt4 Pla2g4b Il3 Fcer1g Pycard Pstpip1 Itga2 Nlrp1a Pla2g4b Fcer1g Grm8 Grm5 Kitl Ccl19 Cxcl11 Cxcr5
Cardiac muscle contraction	Fxyd2 Cacng4 Cacna2d3
Complement activation	Procr Cfi C1rb Cd59a

Reactive astrogliosis genes more than fourfold induced by LPS and grouped by GO enrichment and KEGG enrichment.

hyperphosphorylated Tau-bearing neurons, a neuropathological concept that may have potential therapeutic value. In this study, both insulin and hyperphosphorylated Tau increased in LPS-induced neuroinflammation in vitro and in vivo. Tau hyperphosphorylation and accumulation can be induced by altered insulin signaling (Avila, 2008; Liu et al., 2009), and brain neuroinflammation has been reported to underlie insulin signaling deficits in AD (Bomfim et al., 2012).

In peripheral immune cell, KCa3.1 channels involve in human T cell cytokine release and motility (Chimote et al., 2013). KCa3.1 channels are a part of the immunological synapse signaling complex upon T cell-antigen presentation (Nicolaou et al., 2007). Immunosuppression by *N*-methyl-D-aspartate receptor antagonists is mediated via KCa3.1 channels inhibition in B cells (Simma et al., 2014). KCa3.1 was reported to be involved in the process of reactive astrocytes in CNS (Yu et al., 2014). Expression profiling provides an approach to learning the molecular mechanism of KCa3.1 regulates the phenotype switch of astrogliosis. Our LPS-induced WT and KO reactive astrocyte transcriptomes show that reactive astrocytes undergo extensive gene expression changes between WT-LPS and KO-LPS groups. The transcriptomes included 835 differentially upregulated and 766 differentially downregulated genes with four-fold or greater differences in expression in KO-LPS compared with WT-LPS astrocytes (Fig. 6B). The most prominent were proteins that function in phagosomes (12%), signaling pathways (12%), cell adhesion (11%), neuroactive ligand-receptor interactions (11%), natural killer cell mediated cytotoxicity (8%), and antigen processing and presentation (8%). Our gene profiles strongly suggest that LPS-induced reactive astrocytes are neuroinflammation. They more strongly express high levels of natural killer cell mediated cytotoxicity, antigen processing and presentation, and phagosome, including H2-Q1, H2-T3 and H2-BI. With the gene deletion of KCa3.1, the express levels of H2-Q1, H2-T3 and H2-BI were attenuated in the KO-LPS group. The transcriptomes are consistent with the result that KCa3.1 is indirectly involved in neurotoxicity associated with LPS-induced astrogliosis (Fig. 5).

In this study, both gene deletion and pharmacological blockade of KCa3.1 decreased LPS-induced Tau accumulation and increased insulin receptor expression via the AKT/GSK3β signaling pathway. Pharmacological blockade of KCa3.1 decreased CNS glia inflammation, including reactive astrogliosis and microglial activation. We conclude that KCa3.1 deficiency inhibits LPS-induced proinflammatory responses in primary astrocyte cultures. In vivo KCa3.1 deficiency decreases LPS-induced memory deficits, neuronal loss, glial activation, Tau phosphorylation, and insulin signaling deficits. The data suggest that KCa3.1 has potential as a therapeutic target in neuroinflammation.

Acknowledgements

This work was supported by National Natural Science Foundation of China grant 81773699, Science and Technology Commission of Shanghai Municipality grant 16ZR1418700. The authors declare that the research was conducted in the absence of any commercial or financial relationships that could be construed as a potential conflict of interest. Availability of data and materials Data sharing is not applicable to this article as no datasets were generated or analyzed during the current study.

Authors' contributions

ZY supervised the entire project, designed the research, and wrote the paper. HC conceived and designed the experiments, interpreted and analyzed the data, and supervised all the experimental procedure. TW conceived and designed the experiments, performed the research interpreted, and analyzed the data. QL and YW performed the research and analyzed the data. All authors read and approved the final manuscript.

Ethics approval and consent to participate

The study (ethics protocol number: A-2015-010) was approved by the Animal Care and Use Committee of the Shanghai Jiao Tong University School of Medicine, Shanghai, China.

Declaration of competing interests

The authors declare no competing interest.

Appendix A. Supplementary data

Supplementary data to this article can be found online at https://doi.org/10.1016/j.nbd.2019.104588.

References

Ataga, K.I., Orringer, E.P., Styles, L., Vichinsky, E.P., Swerdlow, P., Davis, G.A., Desimone, P.A., Stocker, J.W., 2006. Dose-escalation study of ICA-17043 in patients with sickle cell disease. Pharmacotherapy 26, 1557–1564.
Avila, J., 2008. Tau kinases and phosphatases. J. Cell. Mol. Med. 12, 258–259.
Bomfim, T.R., Forny-Germano, L., Sathler, L.B., Brito-Moreira, J., Houzel, J.C., Decker, H., Silverman, M.A., Kazi, H., Melo, H.M., McClean, P.L., et al., 2012. An anti-diabetes agent protects the mouse brain from defective insulin signaling caused by Alzheimer's disease- associated Abeta oligomers. J. Clin. Invest. 122, 1339–1353.
Calvo-Ochoa, E., Hernandez-Ortega, K., Ferrera, P., Morimoto, S., Arias, C., 2014. Short-term high-fat-and-fructose feeding produces insulin signaling alterations

accompanied by neurite and synaptic reduction and astroglial activation in the rat hippocampus. J. Cereb. Blood Flow Metab. 34, 1001–1008.

Chimote, A.A., Hajdu, P., Kucher, V., Boiko, N., Kuras, Z., Szilagyi, O., Yun, Y.H., Conforti, L., 2013. Selective inhibition of KCa3.1 channels mediates adenosine regulation of the motility of human T cells. J. Immunol. 191, 6273–6280.

Coulter, D.A., Eid, T., 2012. Astrocytic regulation of glutamate homeostasis in epilepsy. Glia 60, 1215–1226.

Duffy, S.M., Ashmole, I., Smallwood, D.T., Leyland, M.L., Bradding, P., 2015. Orai/CRACM1 and KCa3.1 ion channels interact in the human lung mast cell plasma membrane. Cell Commun. Signal. 13, 32.

Flores, A.I., Narayanan, S.P., Morse, E.N., Shick, H.E., Yin, X., Kidd, G., Avila, R.L., Kirschner, D.A., Macklin, W.B., 2008. Constitutively active Akt induces enhanced myelination in the CNS. J. Neurosci. 28, 7174–7183.

Gao, X., Xia, J., Munoz, F.M., Manners, M.T., Pan, R., Meucci, O., Dai, Y., Hu, H., 2016. STIMs and Orai1 regulate cytokine production in spinal astrocytes. J. Neuroinflammation 13, 126.

Glaser, N., Little, C., Lo, W., Cohen, M., Tancredi, D., Wulff, H., O'Donnell, M., 2017. Treatment with the KCa3.1 inhibitor TRAM-34 during diabetic ketoacidosis reduces inflammatory changes in the brain. Pediatr. Diabetes 18, 356–366.

Hartigan, J.A., Johnson, G.V., 1999. Transient increases in intracellular calcium result in prolonged site-selective increases in Tau phosphorylation through a glycogen synthase kinase 3beta-dependent pathway. J. Biol. Chem. 274, 21395–21401.

Kaushal, V., Koeberle, P.D., Wang, Y., Schlichter, L.C., 2007. The Ca2+ −activated K+ channel KCNN4/KCa3.1 contributes to microglia activation and nitric oxide-dependent neurodegeneration. J. Neurosci. 27, 234–244.

Khakh, B.S., McCarthy, K.D., 2015. Astrocyte calcium signaling: from observations to functions and the challenges therein. Cold Spring Harb. Perspect. Biol. 7, a020404.

Khanna, R., Roy, L., Zhu, X., Schlichter, L.C., 2001. K+ channels and the microglial respiratory burst. Am. J. Phys. Cell Phys. 280, C796–C806.

Kim, B., Figueroa-Romero, C., Pacut, C., Backus, C., Feldman, E.L., 2015. Insulin resistance prevents AMPK-induced tau dephosphorylation through Akt-mediated increase in AMPKSer-485 phosphorylation. J. Biol. Chem. 290, 19146–19157.

Lalo, U., Rasooli-Nejad, S., Pankratov, Y., 2014. Exocytosis of gliotransmitters from cortical astrocytes: implications for synaptic plasticity and aging. Biochem. Soc. Trans. 42, 1275–1281.

Leszek, J., Barreto, G.E., Gasiorowski, K., Koutsouraki, E., Avila-Rodrigues, M., Aliev, G., 2016. Inflammatory mechanisms and oxidative stress as key factors responsible for progression of neurodegeneration: role of brain innate immune system. CNS Neurol. Disord. Drug Targets 15, 329–336.

Li, X., Wu, G., Yang, Y., Fu, S., Liu, X., Kang, H., Yang, X., Su, X.C., Shen, Y., 2017. Calmodulin dissociates the STIM1-Orai1 complex and STIM1 oligomers. Nat. Commun. 8, 1042.

Liddelow, S.A., Barres, B.A., 2017. Reactive astrocytes: production, function, and therapeutic potential. Immunity 46, 957–967.

Liddelow, S.A., Guttenplan, K.A., Clarke, L.E., Bennett, F.C., Bohlen, C.J., Schirmer, L., Bennett, M.L., Munch, A.E., Chung, W.S., Peterson TC, et al., 2017. Neurotoxic reactive astrocytes are induced by activated microglia. Nature 541, 481–487.

Liu, F., Shi, J., Tanimukai, H., Gu, J., Gu, J., Grundke-Iqbal, I., Iqbal, K., Gong, C.X., 2009. Reduced O-GlcNAcylation links lower brain glucose metabolism and tau pathology in Alzheimer's disease. Brain 132, 1820–1832.

Maezawa, I., Zimin, P.I., Wulff, H., Jin, L.W., Feb 4 2011. Amyloid-beta protein oligomer at low nanomolar concentrations activates microglia and induces microglial neurotoxicity. J. Biol. Chem. 286 (5), 3693–3706. https://doi.org/10.1074/jbc.M110.135244.

Meraz-Rios, M.A., Toral-Rios, D., Franco-Bocanegra, D., Villeda-Hernandez, J., Campos-Pena, V., 2013. Inflammatory process in Alzheimer's disease. Front. Integr. Neurosci. 7, 59.

Michaelis, M., Nieswandt, B., Stegner, D., Eilers, J., Kraft, R., 2015. STIM1, STIM2, and Orai1 regulate store-operated calcium entry and purinergic activation of microglia. Glia 63, 652–663.

Moreno, C., Sampieri, A., Vivas, O., Pena-Segura, C., Vaca, L., 2012. STIM1 and Orai1 mediate thrombin-induced Ca(2+) influx in rat cortical astrocytes. Cell Calcium 52, 457–467.

Morris, R., 1984. Developments of a water-maze procedure for studying spatial learning in the rat. J. Neurosci. Methods 11, 47–60.

Newman, E.A., 2015. Glial cell regulation of neuronal activity and blood flow in the retina by release of gliotransmitters. Philos. Trans. R. Soc. Lond. Ser. B Biol. Sci. 370.

Nicolaou, S.A., Neumeier, L., Peng, Y., Devor, D.C., Conforti, L., 2007. The Ca(2+)-activated K(+) channel KCa3.1 compartmentalizes in the immunological synapse of human T lymphocytes. Am. J. Phys. Cell Phys. 292, C1431–C1439.

Pozueta, J., Lefort, R., Shelanski, M.L., 2013. Synaptic changes in Alzheimer's disease and its models. Neuroscience 251, 51–65.

Ramalingam, M., Kim, S.J., 2014. Mechanisms of action of brain insulin against neurodegenerative diseases. J. Neural Transm. (Vienna) 121, 611–626.

Rodriguez-Rodriguez, P., Sandebring-Matton, A., Merino-Serrais, P., Parrado-Fernandez, C., Rabano, A., Winblad, B., Avila, J., Ferrer, I., Cedazo-Minguez, A., 2017. Tau hyperphosphorylation induces oligomeric insulin accumulation and insulin resistance in neurons. Brain 140, 3269–3285.

Schilling, T., Stock, C., Schwab, A., Eder, C., 2004. Functional importance of Ca2+ −activated K+ channels for lysophosphatidic acid-induced microglial migration. Eur. J. Neurosci. 19, 1469–1474.

Schubert, M., Gautam, D., Surjo, D., Ueki, K., Baudler, S., Schubert, D., Kondo, T., Alber, J., Galldiks, N., Kustermann, E., et al., 2004. Role for neuronal insulin resistance in neurodegenerative diseases. Proc. Natl. Acad. Sci. U. S. A. 101, 3100–3105.

Seifert, G., Steinhauser, C., 2013. Neuron-astrocyte signaling and epilepsy. Exp. Neurol. 244, 4–10.

Shapira, R., Solomon, B., Efrati, S., Frenkel, D., Ashery, U., 2018. Hyperbaric oxygen therapy ameliorates pathophysiology of 3xTg-AD mouse model by attenuating neuroinflammation. Neurobiol. Aging 62, 105–119.

Simma, N., Bose, T., Kahlfuss, S., Mankiewicz, J., Lowinus, T., Luhder, F., Schuler, T., Schraven, B., Heine, M., Bommhardt, U., 2014. NMDA-receptor antagonists block B-cell function but foster IL-10 production in BCR/CD40-activated B cells. Cell Commun. Signal. 12, 75.

Sofroniew, M.V., Vinters, H.V., 2010. Astrocytes: biology and pathology. Acta Neuropathol. 119, 7–35.

Sompol, P., Norris, C.M., 2018. Ca(2+), astrocyte activation and calcineurin/NFAT signaling in age-related neurodegenerative diseases. Front. Aging Neurosci. 10, 199.

Song, T.T., Bi, Y.H., Gao, Y.Q., Huang, R., Hao, K., Xu, G., Tang, J.W., Ma, Z.Q., Kong, F.P., Coote, J.H., et al., 2016. Systemic pro-inflammatory response facilitates the development of cerebral edema during short hypoxia. J. Neuroinflammation 13, 63.

Staal, R.G.W., Khayrullina, T., Zhang, H., Davis, S., Fallon, S.M., Cajina, M., Nattini, M.E., Hu, A., Zhou, H., Poda, S.B., et al., 2017. Inhibition of the potassium channel KCa3.1 by senicapoc reverses tactile allodynia in rats with peripheral nerve injury. Eur. J. Pharmacol. 795, 1–7.

Steardo Jr., L., Bronzuoli, M.R., Iacomino, A., Esposito, G., Steardo, L., Scuderi, C., 2015. Does neuroinflammation turn on the flame in Alzheimer's disease? Focus on astrocytes. Front. Neurosci. 9, 259.

Stocker, J.W., De Franceschi, L., McNaughton-Smith, G.A., Corrocher, R., Beuzard, Y., Brugnara, C., 2003. ICA-17043, a novel Gardos channel blocker, prevents sickled red blood cell dehydration in vitro and in vivo in SAD mice. Blood 101, 2412–2418.

Szegedi, V., Juhasz, G., Rozsa, E., Juhasz-Vedres, G., Datki, Z., Fulop, L., Bozso, Z., Lakatos, A., Laczko, I., Farkas, T., et al., 2006. Endomorphin-2, an endogenous tetrapeptide, protects against Abeta1–42 in vitro and in vivo. FASEB J. 20, 1191–1193.

Wei, T., Yi, M., Gu, W., Hou, L., Lu, Q., Yu, Z., Chen, H., 2016. The potassium channel KCa3.1 represents a valid pharmacological target for astrogliosis-induced neuronal impairment in a mouse model of Alzheimer's disease. Front. Pharmacol. 7, 528.

Yi, M., Dou, F., Lu, Q., Yu, Z., Chen, H., 2016a. Activation of the KCa3.1 channel contributes to traumatic scratch injury-induced reactive astrogliosis through the JNK/c-Jun signaling pathway. Neurosci. Lett. 624, 62–71.

Yi, M., Yu, P., Lu, Q., Geller, H.M., Yu, Z., Chen, H., 2016b. KCa3.1 constitutes a pharmacological target for astrogliosis associated with Alzheimer's disease. Mol. Cell. Neurosci. 76, 21–32.

Yi, M., Wei, T., Wang, Y., Lu, Q., Chen, G., Gao, X., Geller, H.M., Chen, H., Yu, Z., 2017. The potassium channel KCa3.1 constitutes a pharmacological target for astrogliosis associated with ischemia stroke. J. Neuroinflammation 14, 203.

Yu, Z.H., Wang, Y.X., Song, Y., Lu, H.Z., Hou, L.N., Cui, Y.Y., Chen, H.Z., 2013. Up-regulation of KCa3.1 promotes human airway smooth muscle cell phenotypic modulation. Pharmacol. Res. 77, 30–38.

Yu, Z., Yu, P., Chen, H., Geller, H.M., 2014. Targeted inhibition of KCa3.1 attenuates TGF-beta-induced reactive astrogliosis through the Smad2/3 signaling pathway. J. Neurochem. 130, 41–49.

Yu, Z., Yi, M., Wei, T., Gao, X., Chen, H., 2017. KCa3.1 inhibition switches the astrocyte phenotype during astrogliosis associated with ischemic stroke via endoplasmic reticulum stress and MAPK signaling pathways. Front. Cell. Neurosci. 11, 319.

Zador, Z., Stiver, S., Wang, V., Manley, G.T., 2009. Role of aquaporin-4 in cerebral edema and stroke. Handb. Exp. Pharmacol. 159–170.

Zakaria, A.S., Rossetti, L., Cristina, M., Veronelli, A., Lombardi, F., Saibene, A., Micheletto, G., Pontiroli, A.E., Group LW, 2016. Effects of gastric banding on glucose tolerance, cardiovascular and renal function, and diabetic complications: a 13-year study of the morbidly obese. Surg. Obes. Relat. Dis. 12, 587–595.

Zamanian, J.L., Xu, L., Foo, L.C., Nouri, N., Zhou, L., Giffard, R.G., Barres, B.A., 2012. Genomic analysis of reactive astrogliosis. J. Neurosci. 32, 6391–6410.